
Article:
Fathima, K.M.P. and de Borst, R. orcid.org/0000-0002-3457-3574 (2019) Implications of single or multiple pressure degrees of freedom at fractures in fluid-saturated porous media. Engineering Fracture Mechanics, 213. pp. 1-20. ISSN 0013-7944

https://doi.org/10.1016/j.engfracmech.2019.03.037

Engineering Fracture Mechanics 213 (2019) 1–20

Contents lists available at ScienceDirect

Engineering Fracture Mechanics

journal homepage: www.elsevier.com/locate/engfracmech

Implications of single or multiple pressure degrees of freedom at fractures in fluid-saturated porous media

K.M. Pervaiz Fathima, René de Borst*

Department of Civil and Structural Engineering, University of Sheffield, Sheffield, United Kingdom

ARTICLE INFO

Keywords:
Crack propagation
Porous media
Fluid pressure
Pressurised fractures
Hydraulic fracturing

ABSTRACT

The physical consequences of modelling the fluid pressure across a fracture using one, two or three degrees of freedom are elucidated. The implications are demonstrated for each model through numerical examples for different boundary value problems. When fracture propagation is mainly driven by mechanical loads a single pressure degree of freedom is normally sufficient. Modelling of the pressure as a discontinuous quantity can be done using a double degree of freedom, similar to the modelling of displacements. Historically, this has been proposed first, but it appears to be less well applicable, except for cases where there is no significant fluid transport along the fracture, as in shear failures. Modelling the pressure with a triple degree of freedom for the pressure at the fracture is the most versatile approach, and is physically the most reasonable and efficient approach to model the propagation of internally pressurised cracks (hydraulic fracturing).

1. Introduction

Modelling fluid flow through fracturing porous media is a challenging multi-scale problem with moving internal boundaries. Moreover, it is an important problem with applications in several fields, ranging from geomechanics to biomedical engineering. Hydraulic fracturing, water retention in dams, aquifers performance, contaminant transport, geological faults and fracture of human tissues are just some examples. In many of these problems, the mechanical and hydraulic behaviour are strongly coupled, resulting in a non-linear response. The problem is complex because of the intertwining of fluid flow inside the fracture with mechanical deformations, and the exchange of fluid between the fracture and the surrounding porous medium.

Analytical approaches are available to model crack propagation in idealised geometries, assuming that the material is linear elastic, homogeneous and impermeable [1–3], typically augmented with an ad hoc leak-off model to account for fluid loss into the surrounding medium under different propagation regimes [4], using linear elastic fracture mechanics [5–7].

Numerical models are essential to realistically capture the behaviour of fracturing porous media for more complicated geometries, for advanced fracture models and/or non-Newtonian fluids. In one of the early models for simulating flow and deformation in fractured or fracturing porous media, the continuum was discretised using finite elements, while the fluid flow inside the fracture was approximated using a finite difference method [8].

Within the class of discrete models to describe fracture interface elements have gained popularity owing to their simplicity and have been extended to fracture in a poroelastic medium [9,10]. While being simple, they suffer from some disadvantages, in particular that they have to be inserted in the mesh a priori, thus restricting their use to cases where the location of the fracture is known

* Corresponding author.
E-mail address: r.deborst@sheffield.ac.uk (R. de Borst).

https://doi.org/10.1016/j.engfracmech.2019.03.037
Received 6 February 2019; Received in revised form 16 March 2019; Accepted 22 March 2019
Available online 26 March 2019

beforehand. The introduction of remeshing has removed this restriction and has enabled the simulation of freely propagating cracks [11–13]. Another approach to crack propagation where the crack path is decoupled from the initial discretisation is the extended finite element method [14–20]. Isogeometric analysis has alleviated other restrictions that adhere to standard finite element analysis, such as the loss of local mass conservation due to the discontinuous character of the pressure gradient and the need for a higher-order interpolation of the fluid pressure in the crack [21,22].

The continuous, or possible discontinuous character of the pressure across the fracture is an important issue in the modelling of fluid flow through fractured, fluid-saturated porous media. It requires a careful consideration and is the main thrust of this contribution. Our aim is to study the physical consequences of assuming the pressure to be either continuous or discontinuous across the fracture. In most of the literature, the pressure is assumed to be continuous across the fracture [15,17,23,24]. Then, a single pressure degree of freedom at the fracture suffices. When interface elements are used, $\mathscr{C}^0$ continuity of the pressure is then automatically enforced, leading to a discontinuity in the pressure gradient, and therefore in the fluid flow. This feature enables fluid to be stored or transported in the crack. When using the extended finite element method, discontinuity of the flow can be achieved by multiplying the pressure by a signed distance function centered at the crack [15,23]. Alternatively, the use of two pressure degrees of freedom at the crack enables the modelling of a discontinuity in the pressure across the crack [10,14]. Evidently, the pressure gradient, and hence the fluid flow, will then exhibit a discontinuity as well. As argued in [25,26], the model of two pressure degrees of freedom is physically less appealing as each of the pressure degrees of freedom is linked to one side of the fracture, with no independent pressure degree available for driving the fluid flow along the fracture. This can be circumvented by defining a third pressure as the average of the two independent pressure degrees of freedom [10], but the number of physically relevant applications of this model seem limited. A technically relevant example where the fluid pressure in the crack is different from that at the sides, and thus, three independent pressure degrees of freedom are necessary, is hydraulic fracturing [19,25,27].

Herein, the three models of a continuous pressure across the fracture, a discontinuous pressure across the interface, and an independent fluid pressure inside the crack are discussed in order to understand the physical consequences of each model as well as their applicability in different contexts. To this end, several cases are examined numerically with different boundary conditions regarding the displacements and the pressure. The three models also present a framework to study the effect of permeability of the interface, which could be different for various applications. For example, opening fractures and dilation bands tend to increase fluid flow along the band whereas compaction bands inhibit flow across the band. Faults on the other hand exhibit more complex behaviour, with an increased permeability along the crack, and a very low permeability across it [28].

Section 2 summarises the governing equations and Section 3 gives the weak format. A concise formulation of the fluid flux along and across the interface is discussed in Section 4. Section 5 presents the used discretisation using poromechanical interface elements with one, two and three pressure degrees of freedom. The physical consequences of considering either format are elucidated next. This discussion includes a comparison of the three models at the hand of several case studies, also covering the applicability of the three options and the effect of the permeability of the interface on the flow pattern and crack propagation characteristics. In particular, it is argued that in order to model a pressurised fracture the option of three independent pressure degrees of freedom is the method of choice, since a single pressure degree of freedom requires an extremely fine mesh near the fracture coupled with an adapted permeability near the crack.

2. Governing equations for the porous medium

We consider a fully saturated porous medium with a solid and a Newtonian fluid (denoted by suffix s and f, respectively) as constituents, subject to the restriction of small variations in concentrations and small displacement gradients. We assume that there is no mass transfer or chemical interaction between the constituents and that the processes occur isothermally. The balance equations for the mixture are obtained by adding the balance equations for each constituent.

Neglecting convective, gravity and inertia terms the balance of linear momentum for a saturated porous medium reads:

$$\nabla\cdot\boldsymbol{\sigma} = \mathbf{0} \tag{1}$$

where $\boldsymbol{\sigma}$ is the total stress, composed of the solid and fluid parts:

$$\boldsymbol{\sigma} = \boldsymbol{\sigma}_s - \alpha p\mathbf{I} \tag{2}$$

where p is the apparent fluid pressure, $\mathbf{I}$ is the unit tensor and α is the Biot coefficient [26]. Using the assumption of small displacement gradients the kinematic relation reads: $\dot{\boldsymbol{\epsilon}}_s = \nabla^s\dot{\mathbf{u}}_s$, with $\dot{\boldsymbol{\epsilon}}_s$ the strain rate field of the solid and $\dot{\mathbf{u}}_s$ the absolute velocity of the solid. The superscript s denotes the symmetric part of the gradient operator. The stress-strain relation is assumed as:

$$\dot{\sigma}_s = \mathbf{D}\colon \dot{\boldsymbol{\epsilon}}_s \tag{3}$$

with $\mathbf{D}$ the fourth-order elastic stiffness tensor.

Using Darcy's relation for flow of Newtonian fluids in an isotropic porous medium,

$$n_f\,\nabla\cdot(\dot{\mathbf{u}}_f - \dot{\mathbf{u}}_s) = -k_f\nabla p \tag{4}$$

with n_f the porosity and k_f the permeability coefficient of the porous medium, the mass balance of the mixture can be written as [26]:

$$\alpha\nabla\cdot\dot{\mathbf{u}}_s - \nabla\cdot(k_f\nabla p) + \frac{1}{M}\frac{\partial p}{\partial t} = 0 \tag{5}$$

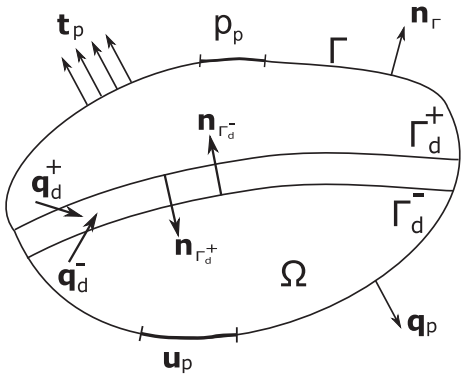

Fig. 1. Body Ω with external boundary Γ and internal boundaries Γ_d^+ and Γ_d^-.

where M is the Biot modulus.

The initial value problem is completed with the following boundary conditions:

$$\mathbf{n}_\Gamma \cdot \boldsymbol{\sigma} = \mathbf{t}_p, \quad \dot{\mathbf{u}}_s = \dot{\mathbf{u}}_p \tag{6}$$

which hold on complementary parts of the boundary Γ_t and Γ_u, respectively, $\mathbf{n}_\Gamma$ being the outward normal vector on the external boundary Γ, Fig. 1. $\mathbf{t}_p$ and $\dot{\mathbf{u}}_p$ are the prescribed external traction and prescribed velocity, respectively. The fluid boundary conditions read:

$$n_f (\dot{\mathbf{u}}_f - \dot{\mathbf{u}}_s) \cdot \mathbf{n}_\Gamma = \mathbf{n}_\Gamma \cdot \mathbf{q}_p, \quad p = p_p \tag{7}$$

which hold on the complementary parts of the boundary Γ_q and Γ_p. $\mathbf{q}_p$ and p_p are the prescribed outflow of the pore fluid and the prescribed pressure respectively. Finally, the initial conditions are:

$$\mathbf{u}_\pi(\mathbf{x}, 0) = \mathbf{u}_\pi^0, \quad \dot{\mathbf{u}}_\pi(\mathbf{x}, 0) = \dot{\mathbf{u}}_\pi^0, \quad p(\mathbf{x}, 0) = p^0, \quad \pi = s, f \tag{8}$$

3. Weak form of the balance equations

The weak form of the balance equations is derived using a standard Bubnov-Galerkin method. We multiply the momentum balance, Eq. (1), and the mass balance, Eq. (5), by kinematically admissible test functions for the displacements of the solid skeleton, $\boldsymbol{\eta}$, and for the pressure ζ, respectively, and integrate over the domain Ω. Using the divergence theorem and taking account of the internal boundaries Γ_d^+ and Γ_d^- as well as the conditions at the external boundaries, Eqs. (6) and (7), lead to the corresponding weak forms:

$$\int_\Omega \nabla\boldsymbol{\eta} : \boldsymbol{\sigma} \mathrm{d}\Omega - \int_{\Gamma_d^+} \boldsymbol{\eta}^+ \cdot (\mathbf{n}_{\Gamma_d^+} \cdot \boldsymbol{\sigma}^+) \mathrm{d}\Gamma - \int_{\Gamma_d^-} \boldsymbol{\eta}^- \cdot (\mathbf{n}_{\Gamma_d^-} \cdot \boldsymbol{\sigma}^-) \mathrm{d}\Gamma = \int_{\Gamma_t} \boldsymbol{\eta} \cdot \mathbf{t}_p \mathrm{d}\Gamma \tag{9}$$

and

$$-\int_\Omega \alpha \zeta \nabla \cdot \dot{\mathbf{u}}_s \mathrm{d}\Omega - \int_\Omega k_f \nabla\zeta . \nabla p \, \mathrm{d}\Omega - \int_\Omega \zeta \frac{1}{M} \frac{\partial p}{\partial \mathrm{t}} \mathrm{d}\Omega - \int_{\Gamma_d^+} \zeta^+ (\mathbf{n}_{\Gamma_d^+} \cdot \mathbf{q}_d^+) \mathrm{d}\Gamma - \int_{\Gamma_d^-} \zeta^- (\mathbf{n}_{\Gamma_d^-} \cdot \mathbf{q}_d^-) \mathrm{d}\Gamma = \int_{\Gamma_t} \zeta \mathbf{n}_\Gamma \cdot \mathbf{q}_p \mathrm{d}\Gamma \tag{10}$$

The presence of the discontinuity inside the domain Ω appears through the power of the external tractions on Γ_d and the normal fluid flux through the faces of the discontinuity. These terms enable the momentum and mass couplings between the discontinuity which is the subgrid scale and the surrounding porous medium, which is the macroscopic scale.

Assuming equilbrium between both faces of the cavity, we have:

$$\boldsymbol{\sigma}^+ \cdot \mathbf{n}_{\Gamma_d^+} = -\boldsymbol{\sigma}^- \cdot \mathbf{n}_{\Gamma_d^-} = \mathbf{t}_d^{\mathrm{loc}} - p\mathbf{n}_{\Gamma_d} \tag{11}$$

where $\mathbf{n}_{\Gamma_d} = \mathbf{n}_{\Gamma_d^-} = -\mathbf{n}_{\Gamma_d^+}$has been used for a zero-thickness interface, see Fig. 1. $\mathbf{t}_d^{\mathrm{loc}}$ are the cohesive tractions in a local coordinate system. Using Eqs. (2) and (11), the balance of linear momentum, Eq. (9), can be reworked as:

$$\int_\Omega \nabla\boldsymbol{\eta} : (\boldsymbol{\sigma}_s - \alpha p \mathbf{I}) \mathrm{d}\Omega + \int_{\Gamma_d} [\![\boldsymbol{\eta}]\!] \cdot (\mathbf{t}_d^{\mathrm{loc}} - p\mathbf{n}_{\Gamma_d}) \mathrm{d}\Gamma = \int_{\Gamma_t} \boldsymbol{\eta} \cdot \mathbf{t}_p \mathrm{d}\Gamma \tag{12}$$

In the local coordinate system, the cohesive tractions $\mathbf{t}_d^{\mathrm{loc}}$ are derived from the relative displacements $[\![\mathbf{u}]\!]$ through a non-linear relation:

$$\mathbf{t}_d^{\mathrm{loc}} = \mathbf{t}_d^{\mathrm{loc}}([\![\mathbf{u}]\!], \kappa) \tag{13}$$

where κ is a history parameter. The traction vector $\mathbf{t}_{\mathbf{d}}^{\mathrm{loc}}$ can be related to the tractions in the global coordinate system using the rotation matrix $\mathbf{R} = (\mathbf{s}_{\Gamma_d}, \mathbf{n}_{\Gamma_d})$, see Fig. 2:

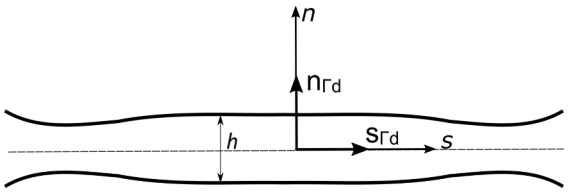

Fig. 2. Geometry and local coordinate system in the cavity.

$$\mathbf{t}_d^{\mathrm{loc}} = \mathbf{R}\mathbf{t}_d \tag{14}$$

For use in a Newton-Raphson iterative procedure, the constitutive relation can be linearised as:

$$\mathrm{d}\mathbf{t}_d^{\mathrm{loc}} = \mathbf{D}_d \mathrm{d}[\![\mathbf{u}]\!] \tag{15}$$

with d denoting a small increment and

$$\mathbf{D}_d = \frac{\partial \mathbf{t}_d^{\mathrm{loc}}}{\partial [\![\mathbf{u}]\!]} \tag{16}$$

Since zero-thickness interface elements are normally placed prior to crack initiation, a finite stiffness is assigned prior to that:

$$\mathbf{D}_d = \begin{bmatrix} d_n & 0 \\ 0 & d_s \end{bmatrix} \tag{17}$$

where d_n and d_s are dummy stiffness values in the normal and tangential directions, respectively. These values must be high to minimise non-physical deformations in the pre-cracking phase [29].

Allowing for the pressure to be discontinuous, and using the definition $\mathbf{n}_{\Gamma_d} = \mathbf{n}_{\Gamma_d^-} = -\mathbf{n}_{\Gamma_d^+}$ for the normals at the discontinuity, the weak form of the mass balance becomes:

$$-\int_\Omega \alpha\zeta\nabla\cdot\dot{\mathbf{u}}_s \mathrm{d}\Omega - \int_\Omega k_f \nabla\zeta.\ \nabla p\, \mathrm{d}\Omega - \int_\Omega \zeta \frac{1}{M}\frac{\partial p}{\partial \mathrm{t}} \mathrm{d}\Omega + \int_{\Gamma_d^+} \zeta^+ (\mathbf{n}_{\Gamma_d}\cdot\mathbf{q}_d^+)\mathrm{d}\Gamma - \int_{\Gamma_d^-} \zeta^- (\mathbf{n}_{\Gamma_d}\cdot\mathbf{q}_d^-)\mathrm{d}\Gamma = \int_{\Gamma_t} \zeta \mathbf{n}_\Gamma\cdot\mathbf{q}_p \mathrm{d}\Gamma \tag{18}$$

while for the case that the pressure p is continuous, so that also ζ is continuous, this expression simplifies to:

$$-\int_\Omega \alpha\zeta\nabla\cdot\dot{\mathbf{u}}_s \mathrm{d}\Omega - \int_\Omega k_f \nabla\zeta.\ \nabla p\, \mathrm{d}\Omega - \int_\Omega \zeta \frac{1}{M}\frac{\partial p}{\partial \mathrm{t}} \mathrm{d}\Omega + \int_{\Gamma_d} \zeta \mathbf{n}_{\Gamma_d}\cdot\Big[\!\Big[\mathbf{q}_d\Big]\!\Big] \mathrm{d}\Gamma = \int_{\Gamma_t} \zeta \mathbf{n}_\Gamma\cdot\mathbf{q}_p \mathrm{d}\Gamma \tag{19}$$

The jump in flux $[\![\mathbf{q}_d]\!] = \mathbf{q}_d^+ - \mathbf{q}_d^-$ is a measure of the net fluid exchange between the fracture and the surrounding porous medium.

4. Fluid flow inside the discontinuity

To obtain the mass coupling term which characterises the jump in flow at the interface, we assume a fully open crack which is filled with Newtonian fluid [15,26]. The crack opening is assumed to be small compared to its length. In a two-dimensional configuration the mass balance for flow within the cavity is given by, see Fig. 2:

$$\frac{\partial v}{\partial s} + \frac{\partial w}{\partial n} = 0 \tag{20}$$

where $v = \dot{\mathbf{u}}_f\cdot\mathbf{s}_{\Gamma_d}$ and $w = \dot{\mathbf{u}}_f\cdot\mathbf{n}_{\Gamma_d}$ are the tangential and normal components of the fluid velocity in the discontinuity, respectively. The difference in the fluid velocity components normal to both crack faces is given by:

$$\Big[\!\Big[w_f\Big]\!\Big] = -\int_{n=-h/2}^{h/2} \frac{\partial v}{\partial s} \mathrm{d}n \tag{21}$$

Combining the momentum balance for the fluid, $\frac{\partial \tau}{\partial n} = \frac{\partial p}{\partial s}$, with τ the shear stress with the constitutive equation for a Newtonian fluid, $\tau = \mu\frac{\partial v}{\partial n}$ with μ the viscosity of the fluid, results in:

$$\mu\frac{\partial^2 v}{\partial n^2} = \frac{\partial p}{\partial s} \tag{22}$$

The velocity profile is obtained by integrating from $n = -h/2$ to $n = h/2$. The boundary condition, i.e. the tangential fluid velocity at the crack face v_f, is obtained by assuming a no-slip condition and using Darcy's relation for the relative fluid velocity in the porous medium at $n = \pm h/2$. Subsituting into Eq. (21) and integrating again with respect to n gives:

$$\Big[\!\Big[w_f\Big]\!\Big] = \frac{1}{12\mu}\frac{\partial}{\partial s}\left(\frac{\partial p}{\partial s}h^3\right) - h\frac{\partial v_f}{\partial s} \tag{23}$$

which is the amount of fluid attracted in the tangential fluid flow and bears similarity to the Reynolds lubrication equation. The

difference in the velocity of solid at the faces of cavity is given by:

$$\left[\!\left[w_s \right]\!\right] = \frac{\partial h}{\partial t} \tag{24}$$

The mass coupling term in Eq. (19) can now be expressed as

$$\mathbf{n}_{\Gamma_d} \cdot \left[\!\left[\mathbf{q}_d \right]\!\right] = \left(\frac{h^3}{12\mu} \frac{\partial^2 p}{\partial s^2} + \frac{h^2}{4\mu} \frac{\partial h}{\partial s} \frac{\partial p}{\partial s} - h \left(\frac{\partial (\dot{u}_s)_s}{\partial s} - \frac{k_f}{n_f} \frac{\partial^2 p}{\partial s^2} \right) - \frac{\partial h}{\partial t} \right) \tag{25}$$

where $(\dot{u}_s)_s$ is the velocity of the solid particles in the local s-direction.

5. Poromechanical interface elements

The standard interface element is augmented with one or more pressure degrees of freedom. Here, we discuss the models of one, two and three pressure degrees of freedom (1PDOF, 2PDOF and 3PDOF). For a single pressure degree of freedom, the pressure is continuous at the internal discontinuity. It is assumed that the pressure on both sides of the discontinuity is equal to the pressure inside it. When two pressure degrees of freedom are added, one on each side of the interface, the pressure can be discontinuous across the internal boundary Γ_d. With three pressure degrees of freedom, the pressure at both sides of the crack are allowed to differ and this can be different from the fluid pressure inside the crack. In all models, the pressure gradient is discontinuous, allowing for storage and fluid flow within the discontinuity because pressure across the interface is at most interpolated in a C^0-continuous manner, yielding a pressure gradient that is C^{-1}- continuous.

5.1. 1PDOF: continuous pressure

We first consider the case of a continuous pressure, see Fig. 3a, so that the pressure in the interface is interpolated as:

$$p = \mathbf{h}_p^{\mathrm{T}} \mathbf{p} \tag{26}$$

where $\mathbf{h}_p^{\mathrm{T}} = (h_{p_1}, ..., h_{p_N})$ contains the interpolation polynomials for the pressure and $\mathbf{p}$ contains the nodal values of the pressure p. We discretise the test function ζ in a Bubnov-Galerkin sense:

$$\zeta = \mathbf{h}_p^{\mathrm{T}} \mathbf{z} \tag{27}$$

with $\mathbf{z}$ the corresponding nodal array. The gradient is given by:

$$\mathbf{B}_p = \begin{bmatrix} \frac{\partial h_{p_1}}{\partial x} & \dots & \dots & \frac{\partial h_{p_N}}{\partial x} \\ \frac{\partial h_{p_1}}{\partial y} & \dots & \dots & \frac{\partial h_{p_N}}{\partial y} \end{bmatrix} \tag{28}$$

From the weak form of balance of momentum, Eq. (12), the equilibrium equation is obtained as:

$$\mathbf{f}_u^{\mathrm{int}} = \mathbf{f}_u^{\mathrm{ext}} \tag{29}$$

where the external force vector is defined as:

$$\mathbf{f}_u^{\mathrm{ext}} = \int_{\Gamma_t} \mathbf{H}^{\mathrm{T}} \mathbf{t}_p \mathrm{d}\Gamma \tag{30}$$

with the matrix $\mathbf{H}$ containing the interpolation polynomials for the displacement $(h_1, ..., h_N)$ as usual, e.g. [26], and the internal force is defined as:

$$\mathbf{f}_u^{\mathrm{int}} = \int_{\Omega} \mathbf{B}_u^{\mathrm{T}} (\boldsymbol{\sigma}_s - \alpha p \mathbf{m}) \mathrm{d}\Omega + \int_{\Gamma_d} \mathbf{B}_d^{\mathrm{T}} (\mathbf{t}_d - p \mathbf{n}_{\Gamma_d}) \mathrm{d}\Gamma \tag{31}$$

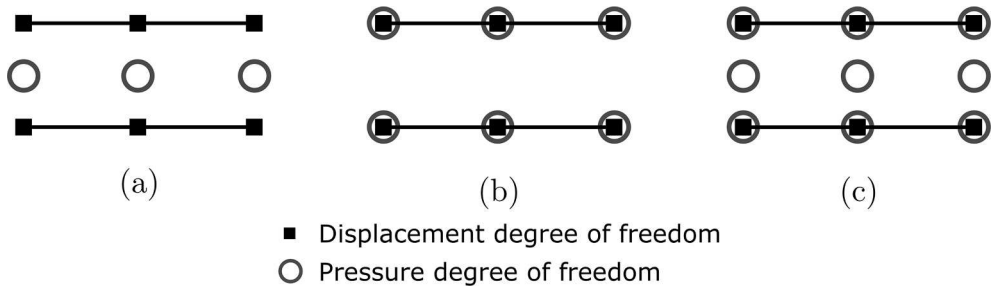

Fig. 3. Zero-thickness interface elements enriched with pressure degrees of freedom (a) 1PDOF (b) 2PDOF (c) 3PDOF.

with $\mathbf{m}^{\mathrm{T}} = (1, 1, 0)$, $\mathbf{B}_u$ the standard strain-nodal displacement matrix, which contains the derivatives of the interpolants for the displacements and $\mathbf{B}_d$ the matrix that sets the relation between the displacement jump at the fracture and the discrete nodal displacement:

$$\mathbf{B}_d = \begin{bmatrix} -\mathbf{h} & +\mathbf{h} & \mathbf{0} & \mathbf{0} \\ \mathbf{0} & \mathbf{0} & -\mathbf{h} & +\mathbf{h} \end{bmatrix} \tag{32}$$

with $\mathbf{h}^{\mathrm{T}} = (h_1, ..., h_N)$.

Linearisation of the internal vector $\mathbf{f}_u^{\mathrm{int}}$, needed for application of the Newton-Raphson procedure, results in:

$$\mathbf{K}_{uu,j-1} = \frac{\partial \mathbf{f}_{u,j-1}^{\mathrm{int}}}{\partial \mathbf{a}} = \underbrace{\int_\Omega \mathbf{B}_u^{\mathrm{T}} \mathbf{D} \mathbf{B}_u \mathrm{d}\Omega}_{\mathbf{K}_{uu,j-1}^{\Omega}} + \underbrace{\int_{\Gamma_d} \mathbf{B}_d^{\mathrm{T}} \mathbf{R}^{\mathrm{T}} \mathbf{D}_{d,j-1} \mathbf{R} \mathbf{B}_d \mathrm{d}\Gamma}_{\mathbf{K}_{uu,j-1}^{\Gamma_d}} \tag{33a}$$

$$\mathbf{K}_{up,j-1} = \frac{\partial \mathbf{f}_{u,j-1}^{\mathrm{int}}}{\partial \mathbf{p}} = -\underbrace{\int_\Omega \alpha \mathbf{B}_u^{\mathrm{T}} \mathbf{m} \mathbf{h}_p^{\mathrm{T}} \mathrm{d}\Omega}_{\mathbf{K}_{up,j-1}^{\Omega}} - \underbrace{\int_{\Gamma_d} \mathbf{B}_d^{\mathrm{T}} \mathbf{n}_{\Gamma_d} \mathbf{h}_p^{\mathrm{T}} \mathrm{d}\Gamma}_{\mathbf{K}_{up,j-1}^{\Gamma_d}} \tag{33b}$$

Next, we substitute the discretisations for the displacement field $\mathbf{u}_s$, for the pressure field p and also for the corresponding test functions in the weak form of mass balance, cf. Eq. (19), and require that the result holds for all admissible test functions. This leads to the discrete format:

$$-\left(\int_\Omega \alpha \mathbf{h}_p \mathbf{m}^{\mathrm{T}} \mathbf{B}_u \mathrm{d}\Omega\right)\dot{\mathbf{a}} - \left(\int_\Omega k_f \mathbf{B}_p^{\mathrm{T}} \mathbf{B}_p \mathrm{d}\Omega\right)\mathbf{p} - \left(\int_\Omega \frac{1}{M} \mathbf{h}_p \mathbf{h}_p^{\mathrm{T}} \mathrm{d}\Omega\right)\dot{\mathbf{p}} + \int_{\Gamma_d} \mathbf{h}_p \mathbf{n}_{\Gamma_d}^{\mathrm{T}} \left[\!\left[\mathbf{q}_d\right]\!\right] \mathrm{d}\Gamma = \int_\Gamma \mathbf{h}_p \mathbf{n}_{\Gamma_d}^{\mathrm{T}} \mathbf{q}_p \mathrm{d}\Gamma \tag{34}$$

The integration over a time step Δt is carried out using the Backward Euler scheme:

$$(\dot{\bullet}) = \frac{(\bullet)^{t+\Delta t} - (\bullet)^t}{\Delta t} \tag{35}$$

Substitution of time integration scheme in the above equation and multiplying with Δt yields:

$$\mathbf{f}_p^{\mathrm{int}} = \mathbf{f}_p^{\mathrm{ext}} \tag{36}$$

with the external force vector:

$$\mathbf{f}_p^{\mathrm{ext}} = \Delta t \int_\Gamma \mathbf{h}_p \mathbf{n}_{\Gamma_d}^{\mathrm{T}} \mathbf{q}_p \mathrm{d}\Gamma \tag{37}$$

and the internal force vector:

$$\begin{aligned} \mathbf{f}_p^{\mathrm{int}} = &-\underbrace{\left(\int_\Omega \alpha \mathbf{h}_p \mathbf{m}^{\mathrm{T}} \mathbf{B}_u \mathrm{d}\Omega\right)}_{-\mathbf{K}_{pu,j-1}^{\Omega} = -\left(\mathbf{K}_{up,j-1}^{\Omega}\right)^{\mathrm{T}}} \mathbf{a}^{t+\Delta t} - \underbrace{\left(\int_\Omega \frac{1}{M} \mathbf{h}_p \mathbf{h}_p^{\mathrm{T}} \mathrm{d}\Omega\right)}_{-\mathbf{M}_{pp,j-1}^{\Omega}} \mathbf{p}^{t+\Delta t} - \underbrace{\left(\Delta t \int_\Omega k_f \mathbf{B}_p^{\mathrm{T}} \mathbf{B}_p \mathrm{d}\Omega\right)}_{-\mathbf{K}_{pp,j-1}^{\Omega}} \mathbf{p}^{t+\Delta t} + \underbrace{\left(\int_\Omega \alpha \mathbf{h}_p \mathbf{m}^{\mathrm{T}} \mathbf{B}_u \mathrm{d}\Omega\right)}_{-\mathbf{K}_{pu,j-1}^{\Omega} = -\left(\mathbf{K}_{up,j-1}^{\Omega}\right)^{\mathrm{T}}} \mathbf{a}^{\mathrm{T}} \\ &+ \underbrace{\left(\int_\Omega \frac{1}{M} \mathbf{h}_p \mathbf{h}_p^{\mathrm{T}} \mathrm{d}\Omega\right)}_{-\mathbf{M}_{pp,j-1}^{\Omega}} \mathbf{p}^{\mathrm{T}} + \Delta t \underbrace{\int_{\Gamma_d} \mathbf{h}_p \mathbf{n}_{\Gamma_d}^{\mathrm{T}} \left[\!\left[\mathbf{q}_d\right]\!\right] \mathrm{d}\Gamma}_{\mathbf{Q}_{\Gamma_d}} \end{aligned} \tag{38}$$

The contributions to the tangential stiffness matrix are obtained by differentiating $\mathbf{f}_p^{\mathrm{int}}$ with respect to $\mathbf{a}$ and $\mathbf{p}$ respectively:

$$\frac{\partial \mathbf{f}_{p,j-1}^{\mathrm{int}}}{\partial \mathbf{a}} = \mathbf{K}_{pu,j-1}^{\Omega} + \Delta t \frac{\partial \mathbf{Q}_{\Gamma_d}}{\partial \mathbf{a}} \tag{39a}$$

$$\frac{\partial \mathbf{f}_{p,j-1}^{\mathrm{int}}}{\partial \mathbf{p}} = \mathbf{M}_{pp,j-1}^{\Omega} + \mathbf{K}_{pp,j-1}^{\Omega} + \Delta t \frac{\partial \mathbf{Q}_{\Gamma_d}}{\partial \mathbf{p}} \tag{39b}$$

The complete linearised set of equations needed in a Newton-Raphson framework, therefore reads:

$$\begin{bmatrix} \mathbf{K}_{uu,j-1}^{\Omega} + \mathbf{K}_{uu,j-1}^{\Gamma_d} & \mathbf{K}_{up,j-1}^{\Omega} + \mathbf{K}_{up,j-1}^{\Gamma_d} \\ \mathbf{K}_{pu,j-1}^{\Omega} + \Delta t \frac{\partial \mathbf{Q}_{\Gamma_d}}{\partial \mathbf{a}}\Big|_{j-1} & M_{pp,j-1}^{\Omega} + \mathbf{K}_{pp,j-1}^{\Omega} + \Delta t \frac{\partial \mathbf{Q}_{\Gamma_d}}{\partial \mathbf{p}}\Big|_{j-1} \end{bmatrix} \begin{pmatrix} \mathrm{d}\mathbf{a} \\ \mathrm{d}\mathbf{p} \end{pmatrix} = \begin{pmatrix} \mathbf{f}_u^{\mathrm{ext}} \\ \mathbf{f}_p^{\mathrm{ext}} \end{pmatrix} - \begin{pmatrix} \mathbf{f}_{u,j-1}^{\mathrm{int}} \\ \mathbf{f}_{p,j-1}^{\mathrm{int}} \end{pmatrix} \tag{40}$$

The terms $\Delta t \frac{\partial \mathbf{Q}_{\Gamma_d}}{\partial \mathbf{a}}$ and $\Delta t \frac{\partial \mathbf{Q}_{\Gamma_d}}{\partial \mathbf{p}}$ render the tangential stiffness matrix non-symmetric, but are pivotal for maintaining (quadratic) convergence and preserving stability of the non-linear iterative procedure in some of the case studies of this paper.

To compute

$$\mathbf{Q}_{\Gamma_d} = \int_{\Gamma_d} \mathbf{h}_p \mathbf{n}_{\Gamma_d}^{\mathrm{T}} \left[\!\left[\mathbf{q}_d \right]\!\right] \mathrm{d}\Gamma \tag{41}$$

we substitute Eq. (25) to result in:

$$\mathbf{Q}_{\Gamma_d} = \int_{\Gamma_d} \mathbf{h}_p \left[\left(\frac{h^3}{12\mu} + h\frac{k_f}{n_f} \right) \frac{\partial^2 p}{\partial s^2} + \frac{h^2}{4\mu} \frac{\partial h}{\partial s} \frac{\partial p}{\partial s} - h\left(\frac{\partial (\dot{u}_s)_s}{\partial s} \right) - \frac{\partial h}{\partial t} \right] \tag{42}$$

where

$$h = \mathbf{n}_{\Gamma_d}^{\mathrm{T}} \mathbf{B}_d \mathbf{a} \tag{43}$$

The derivative of h with respect to s is computed as

$$\frac{\partial h}{\partial s} = \mathbf{n}_{\Gamma_d}^{\mathrm{T}} \mathbf{B}_{d,s} \mathbf{a} \tag{44}$$

with

$$\mathbf{B}_{d,s} = \begin{bmatrix} -\frac{\partial \mathbf{h}}{\partial s} & +\frac{\partial \mathbf{h}}{\partial s} & \mathbf{0} & \mathbf{0} \\ \mathbf{0} & \mathbf{0} & -\frac{\partial \mathbf{h}}{\partial s} & +\frac{\partial \mathbf{h}}{\partial s} \end{bmatrix} \tag{45}$$

For the computation of higher-order derivatives we apply the divergence theorem, resulting in:

$$\mathbf{Q}_{\Gamma_d} = -\int_{\Gamma_d} \left(\frac{h^3}{12\mu} + h\frac{k_f}{n_f} \right) \frac{\partial p}{\partial s} \frac{\partial \mathbf{h}_p}{\partial s} \mathrm{d}\Gamma - \int_{\Gamma_d} \mathbf{h}_p \left(\frac{k_f}{n_f} \frac{\partial h}{\partial s} \frac{\partial p}{\partial s} + h\left(\frac{\partial (\dot{u}_s)_s}{\partial s} \right) + \frac{\partial h}{\partial t} \right) \mathrm{d}\Gamma \tag{46}$$

Next, the tangential gradient of the solid velocity is approximated as the average of the velocities at Γ_d^+ and Γ_d^-:

$$\frac{\partial (\dot{u}_s)_s}{\partial s} \approx \mathbf{s}_{\Gamma_d}^{\mathrm{T}} \bar{\mathbf{B}}_{d,s} \dot{\mathbf{a}} \tag{47}$$

where the operator matrix $\bar{\mathbf{B}}_{d,s}$ is built similar to $\mathbf{B}_{d,s}$ with coefficients ± 1 replaced by $\frac{1}{2}$. Using these identities we obtain,

$$\mathbf{Q}_{\Gamma_d} = \int_{\Gamma_d} -\left(\frac{1}{12\mu} (\mathbf{n}_{\Gamma_d}^{\mathrm{T}} \mathbf{B}_d \mathbf{a})^3 + \frac{k_f}{n_f} (\mathbf{n}_{\Gamma_d}^{\mathrm{T}} \mathbf{B}_d \mathbf{a}) \right) (\mathbf{s}_{\Gamma_d}^{\mathrm{T}} \mathbf{B}_p \mathbf{p}) \frac{\partial \mathbf{h}_p}{\partial s} - \mathbf{h}_p \left(\frac{k_f}{n_f} (\mathbf{n}_{\Gamma_d}^{\mathrm{T}} \mathbf{B}_{d,s} \mathbf{a}) (\mathbf{s}_{\Gamma_d}^{\mathrm{T}} \mathbf{B}_p \mathbf{p}) + (\mathbf{n}_{\Gamma_d}^{\mathrm{T}} \mathbf{B}_d \mathbf{a}) (\mathbf{s}_{\Gamma_d}^{\mathrm{T}} \bar{\mathbf{B}}_{d,s} \dot{\mathbf{a}}) + \mathbf{n}_{\Gamma_d}^{\mathrm{T}} \mathbf{B}_d \dot{\mathbf{a}} \right) \mathrm{d}\Gamma \tag{48}$$

The derivatives of $\mathbf{Q}_{\Gamma_d}$ with respect to $\mathbf{a}$ and $\mathbf{p}$ are:

$$\begin{aligned} \frac{\partial \mathbf{Q}_{\Gamma_d}}{\partial \mathbf{a}} = -\int_{\Gamma_d} & \left(\frac{1}{4\mu} (\mathbf{n}_{\Gamma_d}^{\mathrm{T}} \mathbf{B}_d \mathbf{a})^2 + \frac{k_f}{n_f} \right) (\mathbf{s}_{\Gamma_d}^{\mathrm{T}} \mathbf{B}_p \mathbf{p}) \frac{\partial \mathbf{h}_p}{\partial s} (\mathbf{n}_{\Gamma_d}^{\mathrm{T}} \mathbf{B}_d) + \mathbf{h}_p \left[\frac{k_f}{n_f} (\mathbf{n}_{\Gamma_d}^{\mathrm{T}} \mathbf{B}_{d,s}) (\mathbf{s}_{\Gamma_d}^{\mathrm{T}} \mathbf{B}_p \mathbf{p}) + (\mathbf{n}_{\Gamma_d}^{\mathrm{T}} \mathbf{B}_d) (\mathbf{s}_{\Gamma_d}^{\mathrm{T}} \bar{\mathbf{B}}_{d,s} \dot{\mathbf{a}}) + (\mathbf{n}_{\Gamma_d}^{\mathrm{T}} \mathbf{B}_d \mathbf{a}) \left(\mathbf{s}_{\Gamma_d}^{\mathrm{T}} \bar{\mathbf{B}}_{d,s} \frac{1}{\Delta t} \right) \right. \\ & \left. + \left(\mathbf{n}_{\Gamma_d}^{\mathrm{T}} \mathbf{B}_d \frac{1}{\Delta t} \right) \right] \mathrm{d}\Gamma \end{aligned} \tag{49a}$$

and

$$\frac{\partial \mathbf{Q}_{\Gamma_d}}{\partial \mathbf{p}} = -\int_{\Gamma_d} \left(\frac{1}{12\mu} (\mathbf{n}_{\Gamma_d}^{\mathrm{T}} \mathbf{B}_d \mathbf{a})^3 + \frac{k_f}{n_f} (\mathbf{n}_{\Gamma_d}^{\mathrm{T}} \mathbf{B}_d \mathbf{a}) \right) \frac{\partial \mathbf{h}_p}{\partial s} (\mathbf{s}_{\Gamma_d}^{\mathrm{T}} \mathbf{B}_p) + \mathbf{h}_p [(\mathbf{n}_{\Gamma_d}^{\mathrm{T}} \mathbf{B}_{d,s}) (\mathbf{s}_{\Gamma_d}^{\mathrm{T}} \mathbf{B}_p)] \mathrm{d}\Gamma \tag{49b}$$

5.2. 2PDOF: discontinuous pressure

In case of a discontinuous pressure across the interface element, with p^+ and p^- independent pressure degrees of freedom, see Fig. 3b, the fluid transport across the discontinuity can be formulated as a discrete analogon of Darcy's relation:

$$\mathbf{n}_{\Gamma_d} \cdot \mathbf{q}_d^- = \mathbf{n}_{\Gamma_d} \cdot \mathbf{q}_d^+ = \mathbf{n}_{\Gamma_d} \cdot \mathbf{q}_d = -k_{nd} (p^+ - p^-) = -k_{nd} [\![p]\!] \tag{50}$$

where k_{nd} is the permeability of a diaphragm that is asssumed to coincide with the discontinuity. $k_{nd} = 0$ corresponds to an impervious boundary and $k_{nd} \to \infty$ retrieves the limiting case of continuous pressure ($p^+ = p^-$).

The discretisation of the pressure jump is now similar to that of the displacement jump:

$$[\![p]\!] = (p^+ - p^-) = (\mathbf{h}_p^{\mathrm{T}} \mathbf{p}^+ - \mathbf{h}_p^{\mathrm{T}} \mathbf{p}^-) = \mathbf{H}_p \tilde{\mathbf{p}} \tag{51}$$

with

$$\mathbf{H}_p = [-\mathbf{h}_p^{\mathrm{T}} \quad \mathbf{h}_p^{\mathrm{T}}] \tag{52}$$

The array $\tilde{\mathbf{p}}$ contains discrete nodal pressures at both sides of the interface. Substituting Eq. (51) into Eq. (50) gives:

$$\mathbf{n}_{\Gamma_d}^{\mathrm{T}}\mathbf{q}_d = -k_{nd}\mathbf{H}_p\tilde{\mathbf{p}} \tag{53}$$

An anomaly is now that there is no independent fluid pressure within the crack. As a consequence, the pressure vanishes from the stress continuity condition across the interface, and instead of Eq. (31), the internal force vector becomes:

$$\mathbf{f}_u^{\mathrm{int}} = \int_\Omega \mathbf{B}_u^{\mathrm{T}}(\boldsymbol{\sigma}_s - \alpha p\mathbf{m})\mathrm{d}\Omega + \int_{\Gamma_d}\mathbf{B}_d^{\mathrm{T}}\mathbf{t}_d\mathrm{d}\Gamma \tag{54}$$

Hence, the term $\mathbf{K}_{up}^{\Gamma_d}$ cancels and only the interface term $\mathbf{K}_{uu}^{\Gamma_d}$ given in Eq. (33a) is retained.

The interface term in the weak form of the mass balance, Eq. (18), can be elaborated as:

$$\int_{\Gamma_d^+}\zeta^+(\mathbf{n}_{\Gamma_d}\cdot\mathbf{q}_d^+)\mathrm{d}\Gamma - \int_{\Gamma_d^-}\zeta^-(\mathbf{n}_{\Gamma_d}\cdot\mathbf{q}_d^-)\mathrm{d}\Gamma = -\tilde{\mathbf{z}}^{\mathrm{T}}\int_{\Gamma_d} k_{nd}\mathbf{H}_p^{\mathrm{T}}\mathbf{H}_p\tilde{\mathbf{p}}\mathrm{d}\Gamma \tag{55}$$

where Eq. (53) has been used. Since this expression must hold for all admissible test functions for the pressure, the contribution $\mathbf{Q}_{\Gamma_d}$ which stems from the internal discontinuity to the internal force vector becomes, after multiplication by Δt for symmetry reasons:

$$-\Delta t\left(\int_{\Gamma_d} k_{nd}\mathbf{H}_p^{\mathrm{T}}\mathbf{H}_p\,\mathrm{d}\Gamma\right)\tilde{\mathbf{p}} \tag{56}$$

The complete set of linearised equations needed in a Newton-Raphson iteration therefore is:

$$\begin{bmatrix}\mathbf{K}_{uu,j-1}^{\Omega}+\mathbf{K}_{uu,j-1}^{\Gamma_d} & \mathbf{K}_{up,j-1}^{\Omega}\\ \mathbf{K}_{pu,j-1}^{\Omega} & M_{pp,j-1}^{\Omega}+\mathbf{K}_{pp,j-1}^{\Omega}+\Delta t\frac{\partial\mathbf{Q}_{\Gamma_d}}{\partial\mathbf{p}}\Big|_{j-1}\end{bmatrix}\begin{pmatrix}\mathrm{d}\mathbf{a}\\ \mathrm{d}\mathbf{p}\end{pmatrix} = \begin{pmatrix}\mathbf{f}_u^{\mathrm{ext}}\\ \mathbf{f}_p^{\mathrm{ext}}\end{pmatrix} - \begin{pmatrix}\mathbf{f}_{u,j-1}^{\mathrm{int}}\\ \mathbf{f}_{p,j-1}^{\mathrm{int}}\end{pmatrix} \tag{57}$$

with

$$\frac{\partial\mathbf{Q}_{\Gamma_d}}{\partial\mathbf{p}} = \int_{\Gamma_d} k_{nd}\mathbf{H}_p^{\mathrm{T}}\mathbf{H}_p\,\mathrm{d}\Gamma \tag{58}$$

and all the remaining terms same as in the 1PDOF model.

This model has a deficiency, since the absence of a fluid pressure within the crack precludes fluid transport along the crack. In reality, some assumption for the fluid pressure in the crack must be made. For instance, a linear interpolation can be assumed between p^- and p^+ [10]. However, taking the fluid pressure in the crack as the average of those at the two sides of the cavity makes it impossible, for instance, to model hydraulic fracturing, since then the fluid pressure in the crack must be an independent variable, and is typically larger than that in the surrounding porous medium.

5.3. 3PDOF: independent pressure in the discontinuity

The deficiency of the 2PDOF model can be remedied by explicitly assigning p^- to Γ_d^-, p^+ to Γ_d^+, and p_d to the fluid inside the fracture, using three pressure degrees of freedom, see Fig. 3c. Clearly, the existence of an independent pressure within the discontinuity allows to model the pressurising of a crack, and therefore permits an extension of the modelling capabilities to hydraulic fracturing.

An explicit distinction is now made between the inflow of fluid through the Γ_d^- and Γ_d^+ interfaces. In principle, the resistance at both boundaries can be different. For simplicity, we assume that the resistance is the same at both boundaries of the cavity, k_{nd}. Then, the following relation ensues between the flux into the discontinuity and the different fluid pressures:

$$\mathbf{n}_{\Gamma_d}^{\mathrm{T}}[\![\mathbf{q}_d]\!] = -k_{nd}(p^- - p_d) - k_{nd}(p^+ - p_d) = k_{nd}(2p_d - p^+ - p^-) \tag{59}$$

The sum of pressures p^- and p^+ is interpolated as

$$p^+ + p^- = \mathbf{H}_p\tilde{\mathbf{p}} \tag{60}$$

with $\mathbf{H}_p$ redefined as

$$\mathbf{H}_p = [\mathbf{h}_p^{\mathrm{T}} \quad \mathbf{h}_p^{\mathrm{T}}] \tag{61}$$

Further, there is a separate interpolation for p_d:

$$p_d = \mathbf{h}_d^{\mathrm{T}}\mathbf{p}_d \tag{62}$$

where $\mathbf{h}_d^{\mathrm{T}} = (h_{d_1},\ldots,h_{d_N})$ contains the interpolation polynomials for the pressure in the discontinuity and $\mathbf{p}_d = (p_{d_1},\ldots,p_{d_N})^{\mathrm{T}}$ contains the nodal values of the pressure p_d. We discretise the test function ζ_d for the pressure in the discontinuity in a Bubnov-Galerkin sense:

$$\zeta_d = \mathbf{h}_d^{\mathrm{T}}\mathbf{z}_d \tag{63}$$

with $\mathbf{z}_d$ the corresponding nodal array, and define

$$\nabla p_d = \mathbf{B}_{pd}\mathbf{p}_d \tag{64}$$

with $\mathbf{B}_{pd}$ being the gradient matrix which is assembled in a manner similar to Eq. (28). Using Eqs. (60) and (62), (59) can be written as:

$$\mathbf{n}_{\Gamma_d}^{\mathrm{T}}[\![\mathbf{q}_d]\!] = 2k_{nd}\mathbf{h}_d^{\mathrm{T}}\mathbf{p}_d - k_{nd}\mathbf{H}_p\tilde{\mathbf{p}} \tag{65}$$

Since there is now an independent pressure p_d within the discontinuity, the internal force vector that stems from the momentum balance remains as in the 1PDOF model:

$$\mathbf{f}_u^{\mathrm{int}} = \int_\Omega \mathbf{B}_u^{\mathrm{T}}(\boldsymbol{\sigma}_s - \alpha p\mathbf{m})\mathrm{d}\Omega + \int_{\Gamma_d} \mathbf{B}_d^{\mathrm{T}}(\mathbf{t}_d - p_d\mathbf{n}_{\Gamma_d})\mathrm{d}\Gamma \tag{66}$$

Three separate contributions to the tangential stiffness matrix can now be identified:

$$\mathbf{K}_{uu,j-1} = \frac{\partial \mathbf{f}_{u,j-1}^{\mathrm{int}}}{\partial \mathbf{a}} = \underbrace{\int_\Omega \mathbf{B}_u^{\mathrm{T}}\mathbf{D}\mathbf{B}_u\mathrm{d}\Omega}_{\mathbf{K}_{uu,j-1}^{\Omega}} + \underbrace{\int_{\Gamma_d} \mathbf{B}_d^{\mathrm{T}}\mathbf{R}^{\mathrm{T}}\mathbf{D}_{d,j-1}\mathbf{R}\mathbf{B}_d\mathrm{d}\Gamma}_{\mathbf{K}_{uu,j-1}^{\Gamma_d}} \tag{67a}$$

$$\mathbf{K}_{up,j-1} = \frac{\partial \mathbf{f}_{u,j-1}^{\mathrm{int}}}{\partial \mathbf{p}} = \underbrace{-\int_\Omega \alpha\mathbf{B}_u^{\mathrm{T}}\mathbf{m}\mathbf{h}_p^{\mathrm{T}}\mathrm{d}\Omega}_{-\mathbf{K}_{up,j-1}^{\Omega}} \tag{67b}$$

$$\mathbf{K}_{ud,j-1} = \frac{\partial \mathbf{f}_{u,j-1}^{\mathrm{int}}}{\partial \mathbf{p}_d} = \underbrace{-\int_{\Gamma_d} \mathbf{B}_d^{\mathrm{T}}\mathbf{n}_{\Gamma_d}\mathbf{h}_d^{\mathrm{T}}\mathrm{d}\Gamma}_{-\mathbf{K}_{ud,j-1}^{\Gamma_d}} \tag{67c}$$

After multiplication by Δt, the contributions from global mass balance to the tangential stiffness are obtained as:

$$\mathbf{K}_{pu,j-1} = \frac{\partial \mathbf{f}_{p,j-1}^{\mathrm{int}}}{\partial \mathbf{a}} = \underbrace{-\int_\Omega \alpha\mathbf{h}_p\mathbf{m}^{\mathrm{T}}\mathbf{B}_u\mathrm{d}\Omega}_{-\mathbf{K}_{pu,j-1}^{\Omega}} \tag{68a}$$

$$\mathbf{K}_{pp,j-1} = \frac{\partial \mathbf{f}_{p,j-1}^{\mathrm{int}}}{\partial \mathbf{p}} = \underbrace{-\int_\Omega \frac{1}{M}\mathbf{h}_p\mathbf{h}_p^{\mathrm{T}}\mathrm{d}\Omega}_{-\mathbf{M}_{pp,j-1}^{\Omega}} \underbrace{-\Delta t\int_\Omega k_f\mathbf{B}_p^{\mathrm{T}}\mathbf{B}_p\mathrm{d}\Omega}_{-\mathbf{K}_{pp,j-1}^{\Omega}} \underbrace{-\Delta t\int_\Omega k_{nd}\mathbf{h}_p\mathbf{H}_{pp}\mathrm{d}\Omega}_{-\mathbf{K}_{pp,j-1}^{\Omega}} \tag{68b}$$

$$\mathbf{K}_{pd,j-1} = \frac{\partial \mathbf{f}_{p,j-1}^{\mathrm{int}}}{\partial \mathbf{p}_d} = \underbrace{2\Delta t\int_\Omega k_{nd}\mathbf{h}_p\mathbf{h}_d^{\mathrm{T}}\mathrm{d}\Omega}_{\mathbf{K}_{pd,j-1}^{\Omega}} \tag{68c}$$

where the weak form of Eq. (65) has been exploited and $\mathbf{H}_{pp}$ is defined as:

$$\mathbf{H}_{pp} = \begin{bmatrix} \mathbf{h}_p^{\mathrm{T}} & \mathbf{0} \\ \mathbf{0} & \mathbf{h}_p^{\mathrm{T}} \end{bmatrix} \tag{69}$$

To complete the set of governing equations, the jump in fluid flux in the normal direction given by Eqs. (25) and (59) are combined:

$$2k_{nd}p_d - k_{nd}(p^+ - p^-) - \left(\frac{h^3}{12\mu}\frac{\partial^2 p_d}{\partial s^2} + \frac{h^2}{4\mu}\frac{\partial h}{\partial s}\frac{\partial p_d}{\partial s} - h\left(\frac{\partial(\dot{u}_s)_s}{\partial s} - \frac{k_f}{n_f}\frac{\partial^2 p_d}{\partial s^2}\right) - \frac{\partial h}{\partial t}\right) = 0 \tag{70}$$

with h and $\frac{\partial h}{\partial s}$ as given in Eqs. (43) and (44). After multiplying by the test function ζ_d, integration over Γ_d and application of Gauss' theorem, the following weak form results:

$$\int_{\Gamma_d}\left[2k_{nd}\zeta_d p_d - k_{nd}\zeta_d(p^- + p^+) + \left(\frac{h^3}{12\mu} + \frac{k_f}{n_f}h\right)\frac{\partial\zeta_d}{\partial s}\frac{\partial p_d}{\partial s} + \zeta_d h\frac{\partial(\dot{u}_s)_s}{\partial s} + \zeta_d\frac{\partial h}{\partial t}\right]\mathrm{d}\Gamma = Q_{tip} \tag{71}$$

where Q_{tip} is the inflow of fluid at the crack tip. Multiplication by Δt and discretisation leads to:

$$\mathbf{K}_{du}^{\Gamma_d} = \int_{\Gamma_d} \mathbf{h}_d(h\mathbf{s}_{\Gamma_d}^{\mathrm{T}}\bar{\mathbf{B}}_{d,s} + \mathbf{n}_{\Gamma_d}^{\mathrm{T}}\mathbf{B}_d)\mathrm{d}\Gamma \tag{72a}$$

$$\mathbf{K}_{dp}^{\Gamma_d} = -\Delta t\int_{\Gamma_d} k_{nd}\mathbf{h}_d\mathbf{H}_p\,\mathrm{d}\Gamma \tag{72b}$$

$$\mathbf{K}_{dd}^{\Gamma_d} = \Delta t\int_{\Gamma_d}\left(2k_{nd}\mathbf{h}_d\mathbf{h}_d^{\mathrm{T}} + \left(\frac{h^3}{12\mu} + \frac{k_f}{n_f}h\right)\mathbf{B}_{pd}^{\mathrm{T}}\mathbf{s}_{\Gamma_d}\mathbf{s}_{\Gamma_d}^{\mathrm{T}}\mathbf{B}_{pd}\right)\mathrm{d}\Gamma \tag{72c}$$

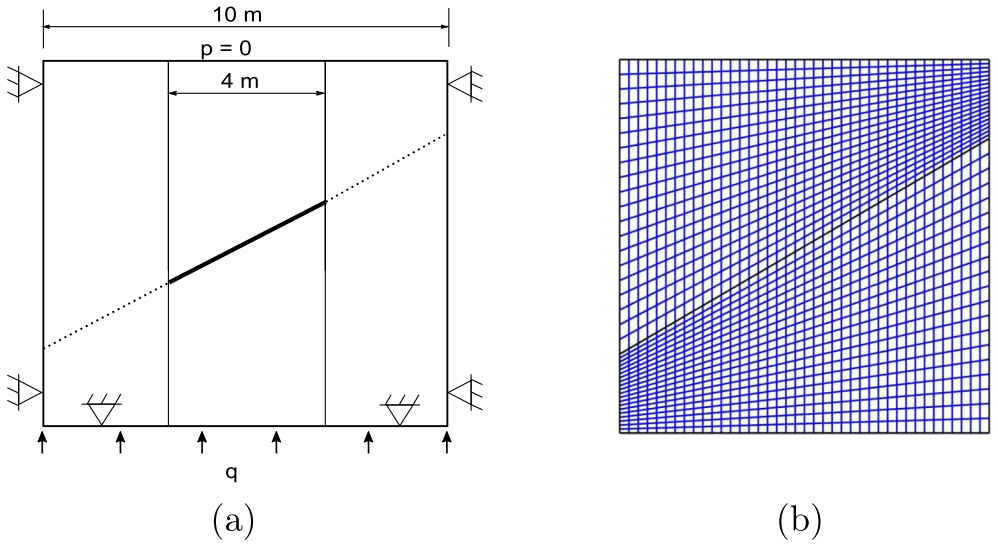

Fig. 4. (a) Geometry and boundary conditions of the square plate (b) Discretisation.

The linearised set of equations then becomes:

$$\begin{bmatrix} \mathbf{K}^{\Omega}_{uu,j-1} + \mathbf{K}^{\Gamma_d}_{uu,j-1} & \mathbf{K}^{\Omega}_{up,j-1} & \mathbf{K}^{\Gamma_d}_{ud,j-1} \\ \mathbf{K}^{\Omega}_{pu,j-1} & \mathbf{M}^{\Omega}_{pp,j-1} + \mathbf{K}^{\Omega}_{pp,j-1} + \mathbf{K}^{\Gamma_d}_{pp,j-1} & \mathbf{K}^{\Gamma_d}_{pd,j-1} \\ \mathbf{K}^{\Gamma_d}_{du,j-1} & \mathbf{K}^{\Gamma_d}_{dp,j-1} & \mathbf{K}^{\Gamma_d}_{dd,j-1} \end{bmatrix} \begin{pmatrix} \mathrm{d}\mathbf{a} \\ \mathrm{d}\mathbf{p} \\ \mathrm{d}\mathbf{p}_d \end{pmatrix} = \begin{pmatrix} \mathbf{f}^{\mathrm{ext}}_{u} \\ \mathbf{f}^{\mathrm{ext}}_{p} \\ \mathbf{f}^{\mathrm{ext}}_{pd} \end{pmatrix} - \begin{pmatrix} \mathbf{f}^{\mathrm{int}}_{u,j-1} \\ \mathbf{f}^{\mathrm{int}}_{p,j-1} \\ \mathbf{0} \end{pmatrix} \tag{73}$$

Similar to the 1PDOF model, the terms at the internal discontinuity render the tangential stiffness matrix unsymmetric.

6. Case studies

We will now study four cases with different loading and boundary conditions. The first case deals with a pre-fractured specimen and the others feature crack propagation under mode I and mode II loading conditions. The three models are compared and the applicability of each model is discussed in different contexts. In all cases, quadratic interpolation functions have been used for the displacements and for the pressure, thus enabling a direct evaluation of the second derivative of the fluid pressure. The interpolation of pressures and displacements with the same polynomial violates the Ladyzhenskaya-Babuška-Brezzi condition, thus opening up the possibility of checkerboard patterns of the pressure to appear. These patterns, however, were not observed in the calculations.

6.1. Square plate with a centre crack

We consider a square plate with a discontinuity inclined at an angle of 30° [22]. A constant flux $q = 10^{-4}$ m/s is imposed on the bottom edge, see Fig. 4a. The material has a Young's modulus $E = 9.0 \times 10^3$ MPa, a Poisson's ratio $\nu = 0.2$, an intrinsic permeability $k = 10^{-12}\,\mathrm{m}^2$, and the fluid has a viscosity $\mu = 10^{-9}$ MPa s. The Biot coefficient $\alpha = 1$, the Biot modulus $M = 10^{18}$ MPa and the porosity $n_f = 0.3$. All boundaries are impermeable except for the top, where fluid is allowed to flow freely. The analysis is carried out using discretisations of 40×40 quadrilateral elements, Fig. 4b, with a time step $\Delta t = 1.0$ s.

Fig. 5 shows the comparison of the pressure distribution between the three models after a steady state has been reached ($t = 40$ s). Fig. 5a shows the pressure distribution for the 1PDOF and 3PDOF models. The crack has opened and the fluid pressure is continuous across the discontinuity in the 1PDOF model and in the 3PDOF model when the interface permeability is greater than or equal to the medium permeability. Fig. 5b shows the pressure distribution for the 2PDOF model when the interface permeability is equal to the permeability of the medium. The pressure is still continuous across the interface. Fig. 5c shows the pressure distribution for the 2PDOF and 3PDOF models when the interface permeability $k_{nd} = 0$. In 2PDOF model, since fluid inside the pressure is not modelled and a zero interface permeability is used, there is no fluid flow across the interface. Fluid is allowed to flow from the sides of the interface and the crack now acts as a barrier for flow. In the 3PDOF model, the fluid pressure inside the interface reduces and approaches zero and therefore the pressure distribution is similar to the 2PDOF model.

Fig. 6 shows the effect of k_{nd} on the pressure inside the discontinuity for the 3PDOF model. When $k_{nd} = k_f$, the pressure inside the discontinuity is the same as that on the bottom and top sides of the interface: the 3PDOF model approaches the 1PDOF model, see also the pressure contours in Fig. 5a. When the interface permeability is reduced, the pressure inside the discontinuity increases, as expected and differences emerge between both models. It is interesting that in the limiting case that the interface is impermeable ($k_{nd} = 0$) the pressure inside the discontinuity approaches zero and behaves like in the 2PDOF model.

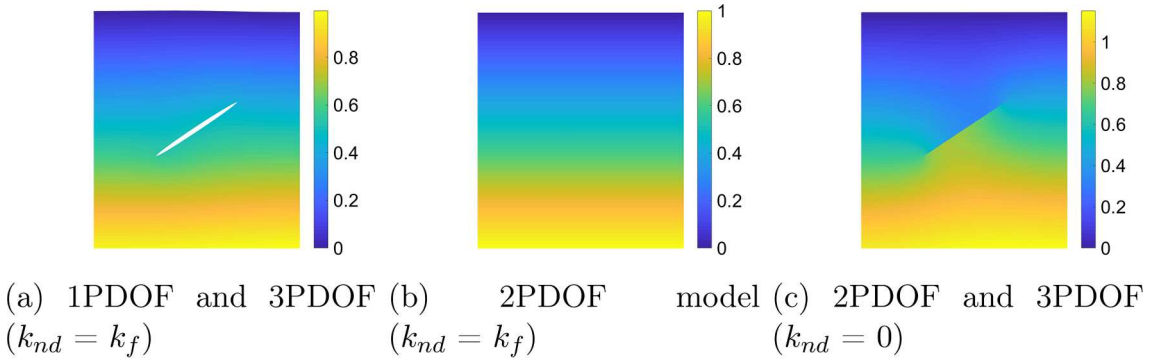

Fig. 5. Pressure distribution in the plate at t = 40 s (units of pressure contours in MPa).

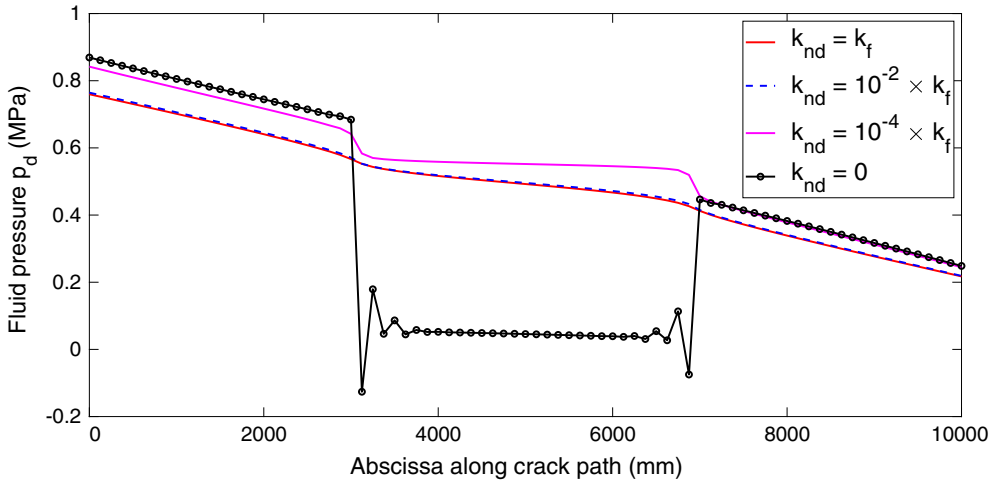

Fig. 6. Pressure inside the discontinuity for different k_{nd} values for the 3PDOF model.

Fig. 7 shows the comparison of the displacement field between all three models after the steady state solution has been reached (at time t = 40 s). Fig. 7a gives the norm of the displacements for the 1PDOF and 3PDOF models with an interface permeability equal to the permeability of the porous medium. Fig. 7b gives the norm of the displacement for the 2PDOF model with an permeability of the interface equal to the permeability of the porous medium. For the 2PDOF model, a high dummy stiffness is used to prevent inter-penetration because fluid inside the crack has not been modelled. Fig. 7c gives the norm of the displacement field for the 2PDOF and the 3PDOF models when the interfaces are assumed to be impermeable, i.e. k_{nd} = 0. Fig. 8 shows the effect of k_{nd} on the displacement on either side of the interface for the 3PDOF model. The displacement on either side of the interface increases upon a reduction of k_{nd}.

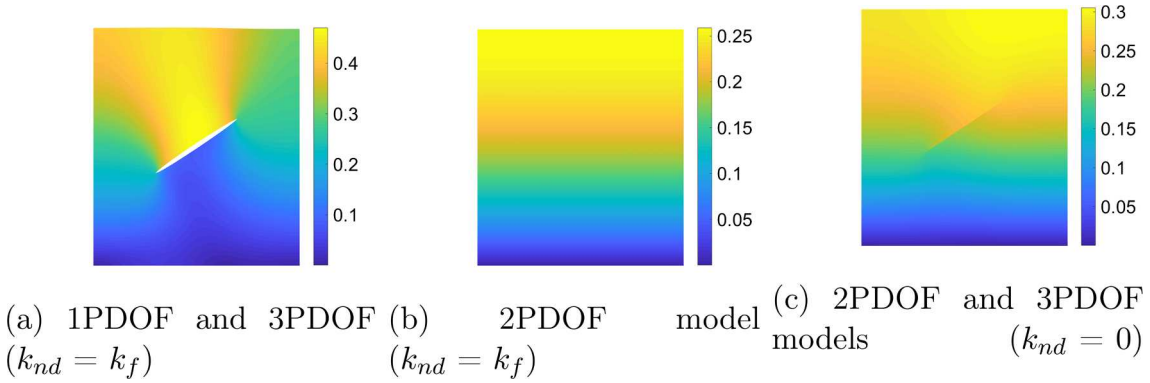

Fig. 7. Displacement norm (in mm) at t = 40 s (magnification factor = 500).

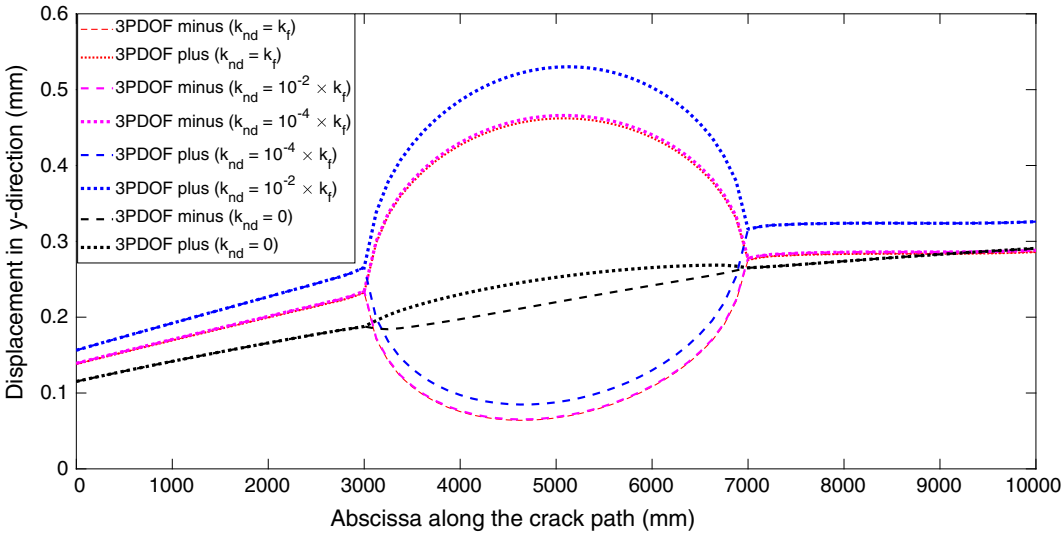

Fig. 8. Effect of k_{nd} for the 3PDOF model.

6.2. Fracture propagation in a single-edge notched plate

We now consider fracture propagation in a pre-notched square plate under plane-strain conditions [30]. The material has a Young's modulus $E = 25.85 \times 10^3$ MPa, Poisson's ratio $\nu = 0.18$, porosity $n_f = 0.2$, and an intrinsic permeability $k = 2.78 \times 10^{-16}$ m^2. The fluid has a viscosity $\mu = 1 \times 10^{-9}$ MPa s. The bulk modulus of the solid material $K_s = 13.46 \times 10^3$ MPa and for the fluid $K_f = 200$ MPa. The Biot coefficient $\alpha = 1$. The plate is 0.25 m long with a 0.05 m notch, see Fig. 9. The plate is subjected to mode-I loading by applying a vertical velocity $v = 23.5 \times 10^{-6}$ m/s at the top and bottom edges. All boundaries of the plate are assumed to be impermeable. The analysis has been carried out using a discretisation of 20×20 quadrilateral elements with a time step of 0.01 s.

Crack propagation is governed by a cohesive zone model. Crack initiation takes place when the traction in the normal direction exceeds the tensile strength of the material. The opening of the crack is governed by an exponential traction-separation relation:

$$t_n = f_t \exp\left(-\frac{f_t}{G_{Ic}}[\![u]\!]_n\right) \tag{74}$$

where t_n and $[\![u]\!]_n$ are the normal traction and jump in displacement, respectively. The tensile strength $f_t = 1.7$ MPa and the mode-I

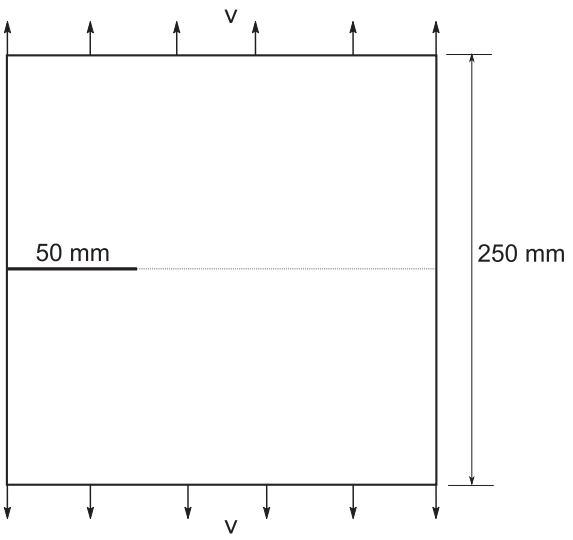

Fig. 9. Fracture propagation in a single-edge notched square plate.

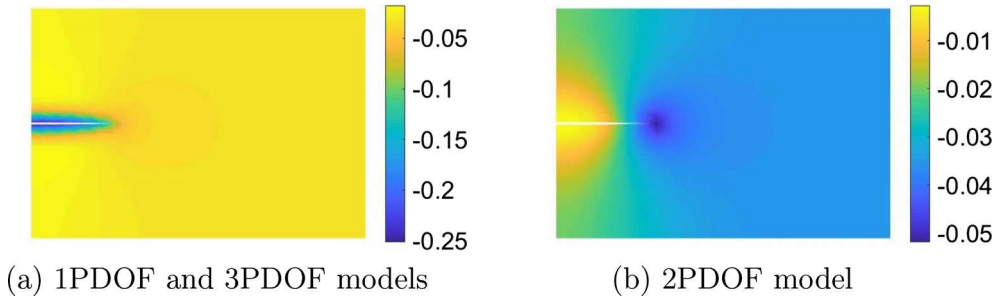

Fig. 10. Pressure distribution at t = 0.2 s (units of pressure contours in MPa).

fracture toughness $G_{Ic} = 100\ \mathrm{J/m^2}$. The permeability of the cohesive zone is assumed to be equal to that of a fully open crack. For the 2PDOF and 3PDOF models the permeability of the interface is taken equal to half the permeability of the bulk.

Fig. 10 shows the pressure distribution at $t = 0.2$ s. The 1PDOF and 3PDOF models with a high interface permeability yield the same results. Physically this does not constitute a very meaningful case, but it confirms that the 3PDOF model then coincides with the 1PDOF model. However, when interface permeability is taken equal to half the permeability of the bulk, the pressures along the fracture are lower than the pressure inside, see Fig. 11, where the pressure along the crack is shown on both sides of the interface for all models at $t = 0.2$ s.

Fig. 12 shows the displacement in the y-direction at 0.2 s for all three models. The displacement on either side of the fracture is the highest in the 2PDOF model. The 1PDOF model and the 3PDOF model with a high interface permeability yield identical results. When k_{nd} is equal to half of the permeability of the medium, the displacement is smaller than for the continuous pressure.

6.3. Shear-band formation

Next we consider a two-dimensional specimen with a width $w = 0.04$ m and a height $H = 0.1$ m, which is loaded under plane-strain conditions [14]. The sides are traction-free and the external loading is applied via an imposed constant velocity $v = -10^{-4}$ m/s at the top edge, see Fig. 13. The pore pressure at the top of the specimen is zero, and undrained boundary conditions are imposed at the other boundaries. The material has a Young's modulus $E = 20^3$ MPa and a Poisson's ratio $\nu = 0.35$. The Biot coefficient $\alpha = 1$ and the Biot modulus $M = 5 \times 10^3$ MPa. The bulk material has a permeability $k_f = 10^{-11}\ \mathrm{m^3/N\,s}$. Shear-band formation is triggered by a small imperfection, see Fig. 13. Interface elements have been inserted along a 45° angle starting from the imperfection. The permeability of the interface is half of that in the bulk material. Simulations have been carried out using 24×60 quadrilateral elements. A time step $\Delta t = 0.4$ s has been used.

The failure mode involves only sliding and no opening. A cohesive zone model governs the crack propagation in mode II. The following linear traction-sliding relation has been used:

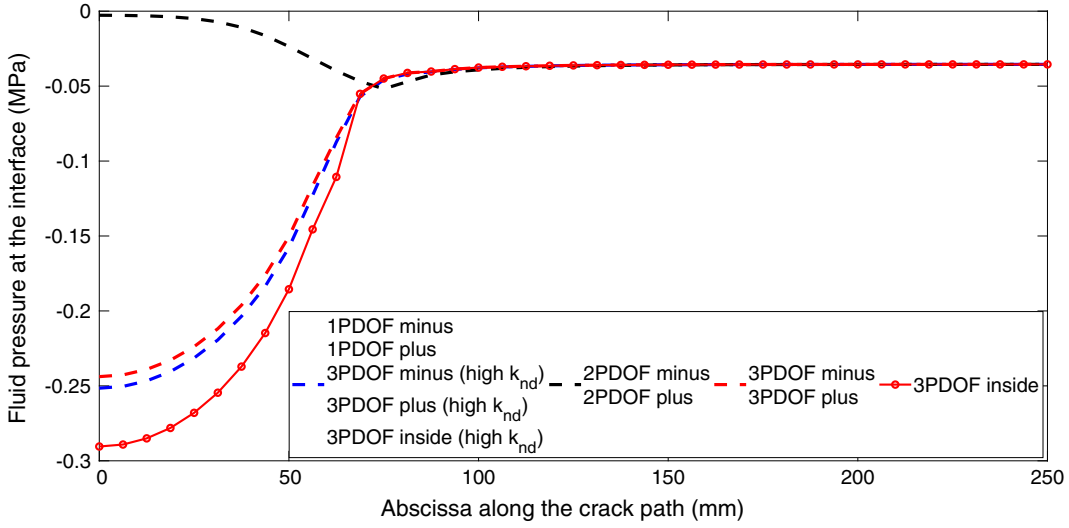

Fig. 11. Pressure along the interface at $t = 0.2$ s.

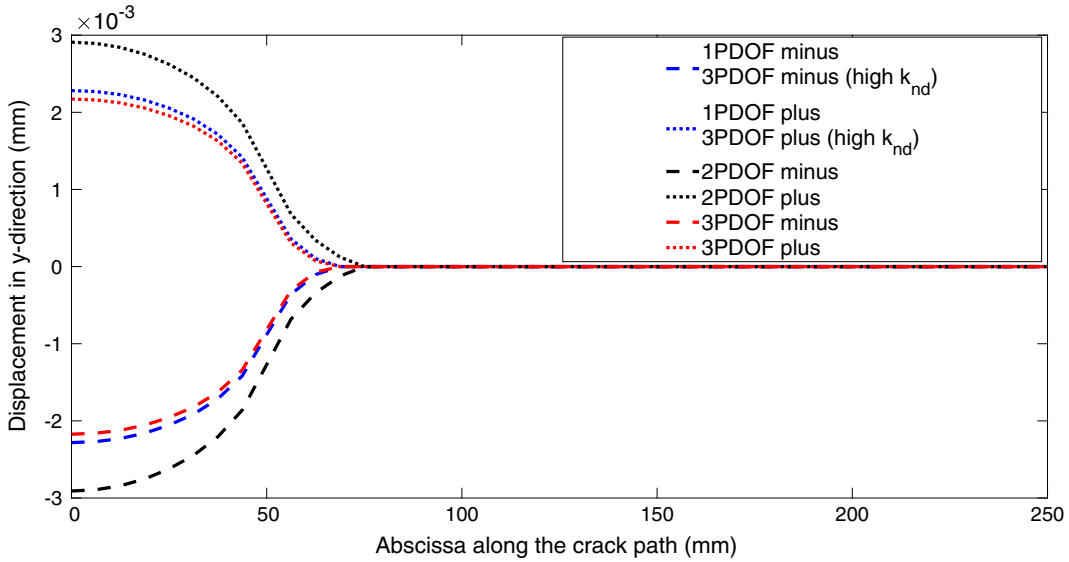

Fig. 12. Displacement in the *y*-direction along the interface at time t = 0.2 s.

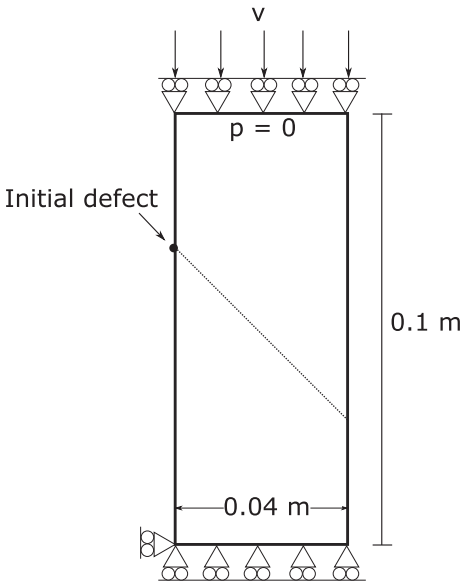

Fig. 13. Geometry and boundary conditions.

$$t_s = \tau_c \left(1 - \frac{|[\![u]\!]_s|}{\delta_{cr}}\right) \mathrm{sgn}([\![u]\!]_s) \tag{75}$$

where t_s and $[\![u]\!]_s$ are the traction and the jump of the displacement in the tangential direction, respectively. The critical shear stress that governs crack initiation, τ_c has been taken equal to 100 MPa and after inception, the shear-band evolution is controlled by the mode II fracture energy, $G_{IIc} = 500\ \mathrm{J/m^2}$. δ_{cr} is the critical displacement when the shear stress is zero given by $2G_{IIc}/\tau_c$. If the direction of shearing is reversed at $|[\![u]\!]_{s1}| < \delta_{cr}$, the shear traction is assumed to follow a secant unloading/reloading relation.

Fig. 14 shows the pressure distribution for the 1PDOF model at 4 s, 6.4 s, 7.6 s and 8 s. The pressure across the interface is now continuous. Similarly, Figs. 15 and 16 show the pressure contours for the 2PDOF and 3PDOF models, respectively. Evidently, the pressure across the crack is now discontinuous. Fig. 17 shows the comparison between the three models at $t = 6.4$ s. The displacement profile is the same for all three models, Fig. 17a. Fig. 17b shows that the pressure in the 1PDOF model is equal to the pressure inside the discontinuity of the 3PDOF model. The pressure on either side of the interface is higher than pressure inside the discontinuity. The pressure inside the fracture is not captured explicitly in the 2PDOF model, but a discontinuity in the pressure across the crack clearly shows up. The permeability of the interface for the 2PDOF and 3PDOF models is taken equal to half the permeability of the bulk. Since the crack opening is zero, the 2PDOF and 3PDOF models are essentially the same. In the 2PDOF model there is a jump in

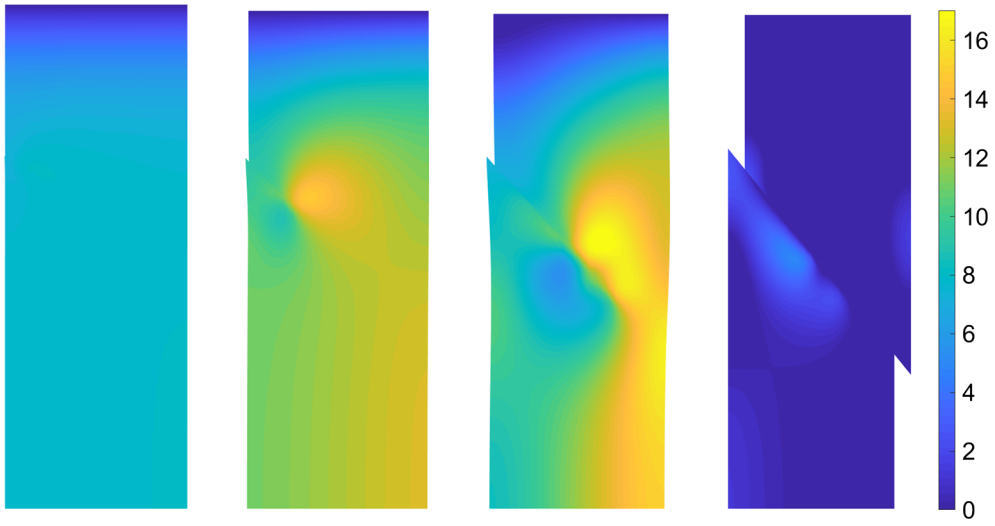

Fig. 14. Pressure distribution (in MPa) at 4 s, 6.4 s, 7.6 s and 8 s for the 1PDOF model (magnification factor = 5).

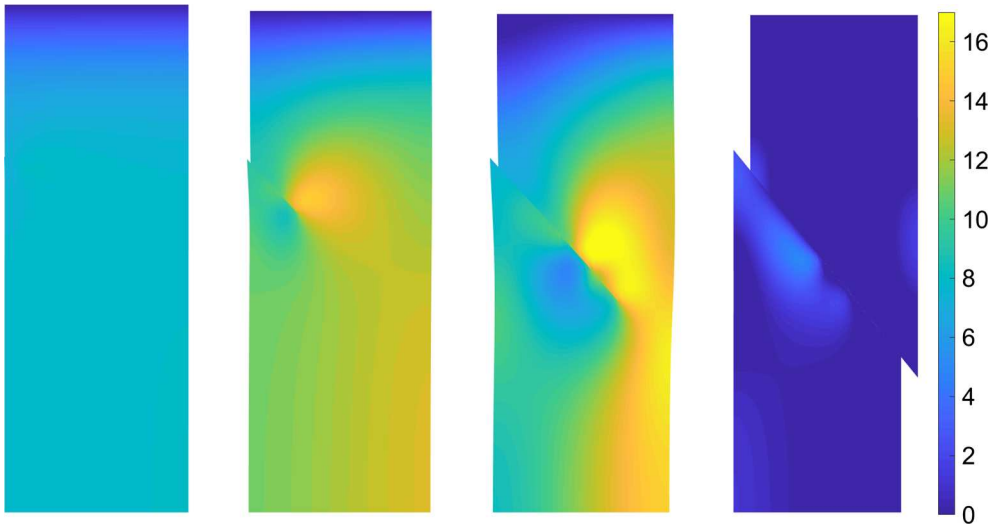

Fig. 15. Pressure distribution (in MPa) at 4 s, 6.4 s, 7.6 s and 8 s for the 2PDOF model (magnification factor = 5).

pressure from the minus to the plus side of the interface and the flux is dependent on the coefficient k_{nd}. In the 3PDOF model there is a jump in the pressure from the minus side to the interior of the discontinuity and again a jump from the plus side to the interior of the discontinuity. The flux is dependent on the interface permeability k_{nd}, and in the 3PDOF model an increase in k_{nd} results in the same pressure distribution as in the 2PDOF model. Fig. 18 shows the effect of increasing k_{nd}, yielding identical results for the 2PDOF and 3PDOF models.

6.4. Pressurised fracture

We reconsider the specimen of Section 6.2 with the same material properties, but with different loading and boundary conditions. Fluid is injected at the inlet of the pre-existing notch at a constant rate $Q_{in} = 5 \times 10^{-5}\,\mathrm{m}^2/\mathrm{s}$. The pressure is zero at the top, bottom and right boundaries. The displacement in the x-direction is constrained at the right boundary and the rightmost tip of crack path is constrained in the y-direction, see Fig. 19. The mesh size and the time step are the same as that given in Section 6.2. Again, a cohesive zone model with an exponential traction-separation relation has been used.

Fig. 20 shows the pressure variation for the 1PDOF and 3PDOF models. The pressures are higher in the 1PDOF model compared to the 3PDOF model when the permeability of the interface is equal to that of the porous medium. This is seen in Fig. 21a, which shows the pressure along the plus and minus sides of the interface for the 1PDOF and 3PDOF models together with the pressure inside the

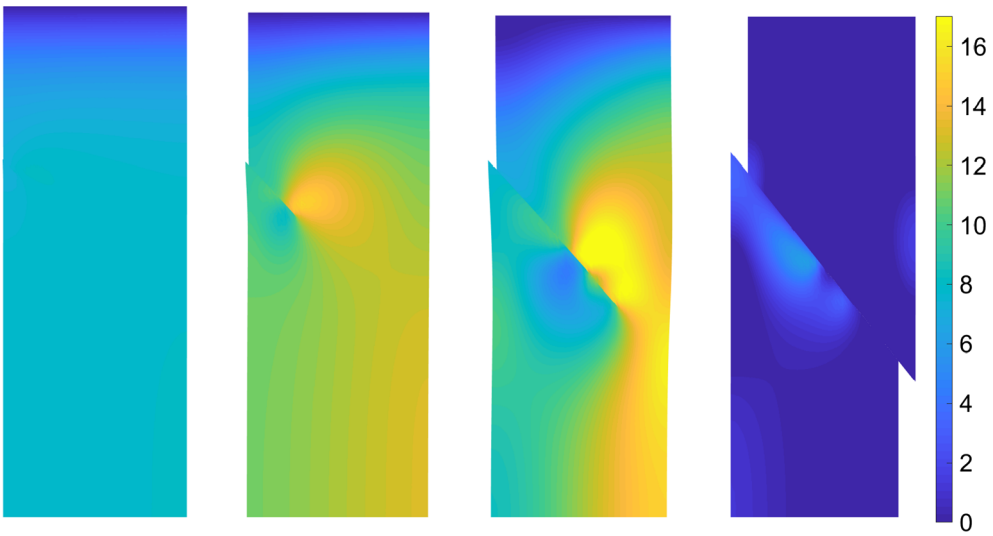

Fig. 16. Pressure distribution (in MPa) at 4 s, 6.4 s, 7.6 s and 8 s for the 3PDOF model (magnification factor = 5).

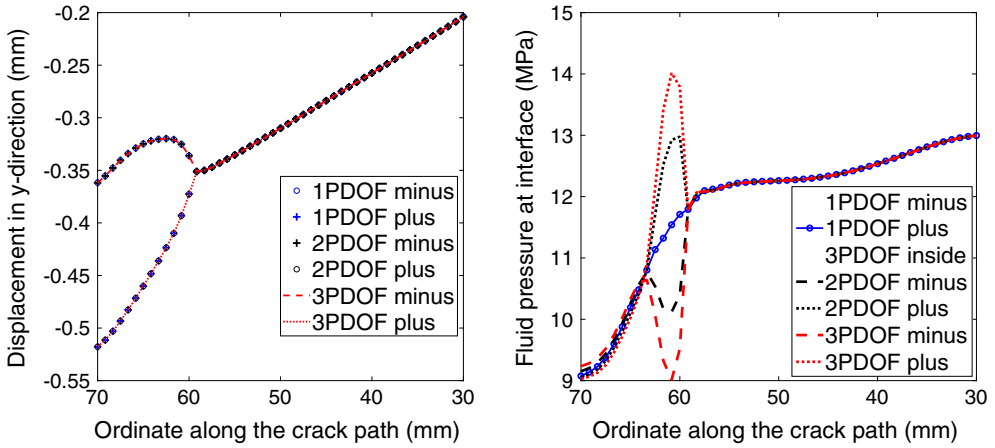

(a) Displacement in the y-direction (b) Fluid pressure

Fig. 17. (a) Displacement in the y-direction and (b) pressure variation along the crack path at time 6.4 s.

discontinuity. For the 3PDOF model the pressure inside the crack is higher than the pressure on either side of the interface. When the permeability of the interface k_{nd} is increased, the pressures become continuous across the interface and approaches those of the 1PDOF model.

Fig. 21b shows the displacement along the plus and minus sides of the interface for the 1PDOF and 3PDOF models. The displacements in the 3PDOF model are higher than those in the 1PDOF model. This is because of higher pressure inside the discontinuity for the 3PDOF model. For higher values of the permeability of the interface, the 3PDOF model yields the same results as the 1PDOF model.

Fig. 22a shows the increase in crack length with time for the 1PDOF and 3PDOF models. The crack length is slightly higher in the 3PDOF model compared to the model with a continuous pressure. For lower values of the permeability of the interface, the crack propagation becomes faster. Fig. 22b gives the variation of the crack opening at the left edge with time for the 1PDOF and the 3PDOF models. The crack opening is higher in the 3PDOF model compared to the model with the continuous pressure. This is attributed to the higher pressure inside the discontinuity compared to the pressure at the faces in the case of the 3PDOF model. When the permeability of the interface is reduced, the crack opening increases because of the larger fluid pressure inside the fracture.

Fig. 22a also shows an increase in crack length which seems to be stepwise [31]. While it is physically quite well possible that such a phenomenon exists, and there is evidence from simulations using *discrete* models [32], it may be less likely that a *continuum* model can predict such a discrete phenomenon. Indeed, Fig. 23 suggests that the stepwise propagation disappears upon refinement of the discretisation and the time step.

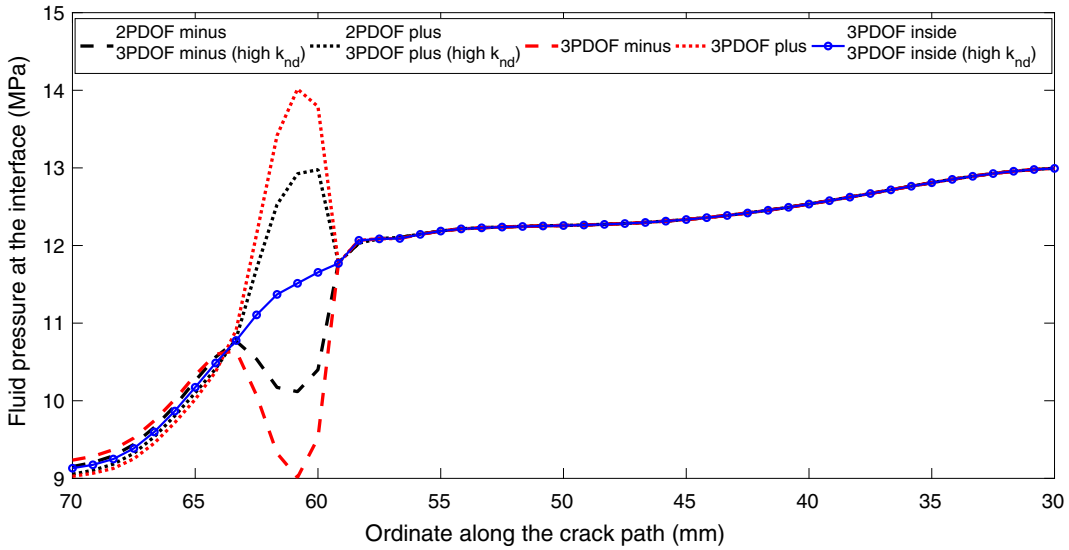

Fig. 18. Effect of k_{nd} on pressure.

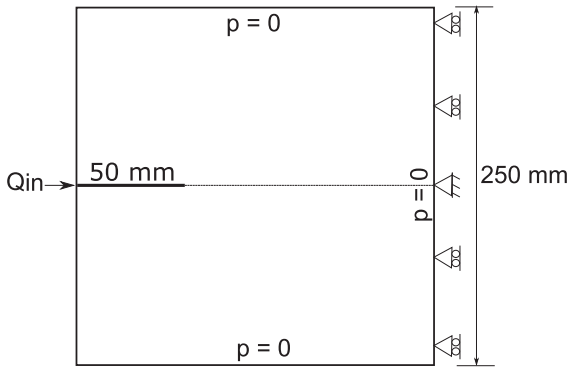

Fig. 19. Pressurised fracture.

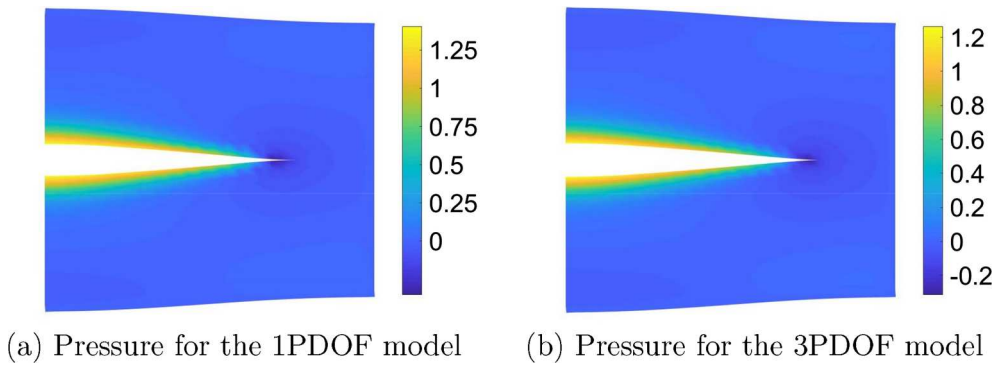

Fig. 20. Pressure distribution (in MPa) at t = 0.2 s (magnification factor = 500).

7. Concluding remarks

Three different interpolations of the fluid pressure across a fracture have been examined in order to understand the physical consequences and the applicability in different contexts through numerical case studies. In all models, the pressure gradient is discontinuous, thus enabling the exchange of fluid between the discontinuity and the surrounding porous bulk material.

The one pressure degree of freedom model assumes the pressure to be continuous across the fracture. This model is applicable

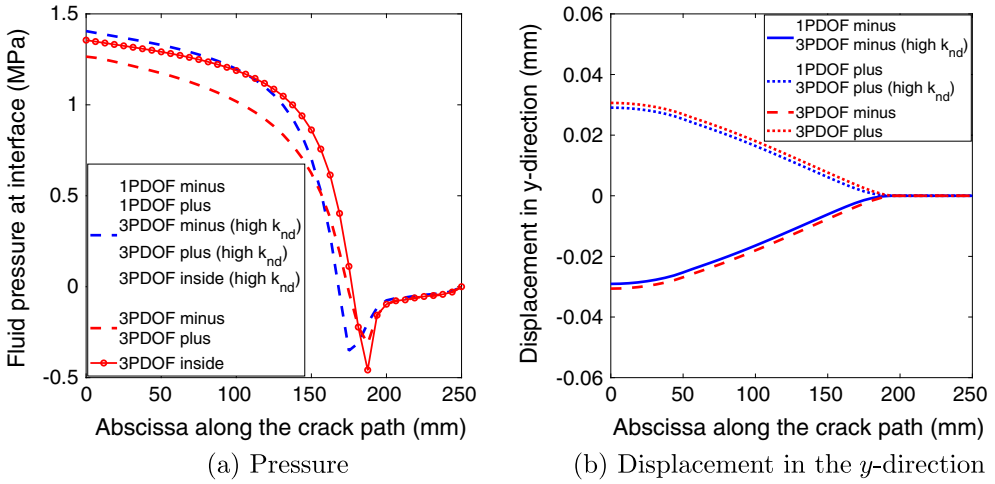

(a) Pressure (b) Displacement in the y-direction

Fig. 21. Pressures and displacement along the interface at t = 0.2 s.

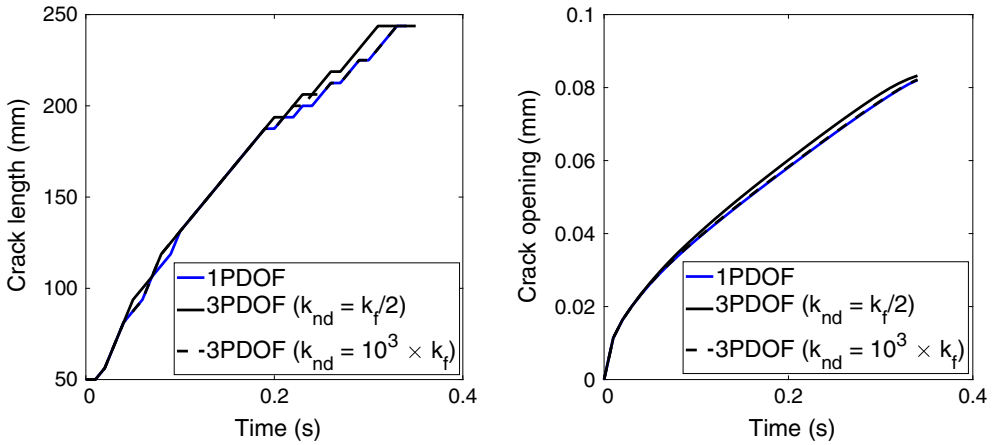

(a) Crack length (b) Crack opening

Fig. 22. Crack length and crack opening at the left edge.

when the pressure inside the crack is equal to the pressure at the faces of crack. When the crack is not internally pressurised this model can be used. A two pressure degrees of freedom model can capture a discontinuity in the pressure across the fracture. However, the pressure inside the discontinuity is not modelled and no fluid transport along the fracture is now possible. For that, an independent pressure inside the fracture must be assumed, different from the pressure at the faces of the discontinuity. This three pressure degrees of freedom model is the most versatile and can handle both continuous and discontinuous pressures through suitable values for the permeability of the interface.

The permeability of the interface influences the crack propagation speed, with a lower value resulting in faster crack propagation. It is observed that the pressure inside the discontinuity is different from the pressure on the faces of the discontinuity. In the cases where a displacement boundary condition is applied, fluid flows from the bulk to the cavity and hence the fluid pressure inside the fracture is lower than the pressure at the sides of the discontinuity. On the contrary, for a pressurised fracture, the pressure inside the discontinuity is higher than that on either side of the discontinuity.

While the three pressure degree of freedom model is the most versatile approach, the single degree of freedom pressure model can, in principle, also be used for applications like hydraulic fracturing. But this comes at a price, since extremely fine discretisations near the fracture must be applied, in conjunction with a different permeability close to the fracture in order to properly take into account the leak-off effect. Therefore, a three pressure degree of freedom model with a judiciously chosen leak-off coefficient is much more efficient since it leads to a considerably smaller number of degrees of freedom.

The contributions from the fluid flux term across the discontinuity lead to an unsymmetric tangential stiffness matrix. Yet, their inclusion is essential for the stability of the solution and a quadratic convergence of the Newton-Raphson iterative procedure.

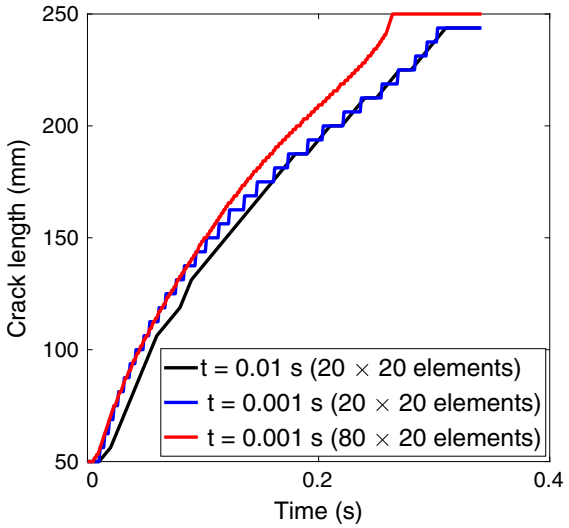

Fig. 23. Crack length evolution for mesh refinement and smaller time steps. The 3PDOF model has been used with an interface permeability $k_{nd} = k_f/2$.

Acknowledgement

The research reported in this manuscript has been supported by the European Research Council (Advanced Grant 664734 'PoroFrac').

Appendix A. Supplementary material

Supplementary data associated with this article can be found, in the online version, at https://doi.org/10.1016/j.engfracmech.2019.03.037.

References

[1] Perkins TK, Kern LR. Widths of hydraulic fractures. J Petrol Technol 1961;13:937–49.
[2] Geertsma J, De Klerk F. A rapid method of predicting width and extent of hydraulically induced fractures. J Petrol Technol 1969;21:1571–81.
[3] Nordgren RP. Propagation of a vertical hydraulic fracture. SPE J 1972;12:306–14.
[4] Carter RD. Derivation of the general equation for estimating the extent of the fractured area. Appendix I of optimum fluid characteristics for fracture extension. In: Drilling and production practice. Tulsa, Oklahoma: API; 1957. p. 261–70.
[5] Bunger AP, Detournay E, Garagash DI. Toughness-dominated hydraulic fracture with leak-off. Int J Fract 2005;134:175–90.
[6] Garagash DI, Detournay E. Plane-strain propagation of a fluid-driven fracture: small toughness solution. J Appl Mech 2005;72:916–28.
[7] Adachi JI, Detournay E. Plane strain propagation of a hydraulic fracture in a permeable rock. Eng Fract Mech 2008;75:4666–94.
[8] Boone TJ, Ingraffea AR. A numerical procedure for simulation of hydraulically-driven fracture propagation in poroelastic media. Int J Numer Anal Meth Geomech 1990;14:27–47.
[9] Segura JM, Carol I. On zero-thickness interface elements for diffusion problems. Int J Numer Anal Methods Geomech 2004;28:947–62.
[10] Segura JM, Carol I. Coupled HM analysis using zero-thickness interface elements with double nodes. Part I: theoretical model. Int J Numer Anal Meth Geomech 2008;32:2083–101.
[11] Sousa JLS, Carter BJ, Ingraffea AR. Numerical simulation of 3D hydraulic fracture using Newtonian and power-law fluids. Int J Rock Mech Min Sci 1993;30:1265–71.
[12] Carter BJ, Desroches J, Ingraffea AR, Wawrzynek PJ. Simulating fully 3D hydraulic fracturing. In: Zaman M, Gioda G, Booker J, editors. Modeling in geomechanics. Chichester: J. Wiley & Sons; 2000. p. 525–57.
[13] Secchi S, Simoni L, Schrefler BA. Mesh adaptation and transfer schemes for discrete fracture propagation in porous materials. Int J Numer Anal Meth Geomech 2007;31:331–45.
[14] de Borst R, Réthoré J, Abellan MA. A numerical approach for arbitrary cracks in a fluid-saturated medium. Arch Appl Mech 2006;75:595–606.
[15] Réthoré J, de Borst R, Abellan MA. A two-scale approach for fluid flow in fractured porous media. Int J Numer Meth Eng 2007;71:780–800.
[16] Lecampion B. An extended finite element method for hydraulic fracture problems. Commun Numer Methods Eng 2009;25:121–33.
[17] Mohammadnejad T, Khoei AR. Hydro-mechanical modelling of cohesive crack propagation in multiphase porous media using the extended finite element method. Int J Numer Anal Meth Geomech 2013;37:1247–79.
[18] Gordeliy E, Peirce A. Coupling schemes for modeling hydraulic fracture propagation using the XFEM. Comput Methods Appl Mech Eng 2013;253:305–22.
[19] Remij EW, Remmers JJC, Huyghe JM, Smeulders DMJ. The enhanced local pressure model for the accurate analysis of fluid pressure driven fracture in porous materials. Comput Methods Appl Mech Eng 2015;286:293–312.
[20] Prévost JH, Sukumar N. Fault simulations for three-dimensional reservoir-geomechanical models with the extended finite element method. J Mech Phys Solids 2016;86:1–18.
[21] Irzal F, Remmers JJC, Verhoosel CV, de Borst R. An isogeometric analysis Bézier interface element for mechanical and poromechanical fracture problems. Int J Numer Meth Eng 2014;97:608–28.
[22] Vignollet J, May S, de Borst R. Isogeometric analysis of fluid-saturated porous media including flow in the cracks. Int J Numer Meth Eng 2016;108:990–1006.
[23] Réthoré J, de Borst R, Abellan MA. A two-scale model for fluid flow in an unsaturated porous medium with cohesive cracks. Comput Mech 2008;42:227–38.

[24] Carrier B, Granet S. Numerical modeling of hydraulic fracture problem in permeable medium using cohesive zone model. Eng Fract Mech 2012;79:312–28.
[25] de Borst R. Fluid flow in fractured and fracturing porous media: a unified view. Mech Res Commun 2017;80:47–57.
[26] de Borst R. Computational methods for fracture in porous media. New York: Elsevier; 2018.
[27] Nguyen VP, Lian H, Rabczuk T, Bordas S. Modelling hydraulic fractures in porous media using flow cohesive interface elements. Eng Geol 2017;225:68–82.
[28] Foster CD, Nejad TM. Embedded discontinuity finite element modeling of fluid flow in fractured porous media. Acta Geotech 2013;8:49–57.
[29] Schellekens JCJ, de Borst R. On the numerical integration of interface elements. Int J Numer Meth Eng 1993;36:43–66.
[30] Irzal F, Remmers JJC, Huyghe JM, de Borst R. A large deformation formulation for fluid flow in a progressively fracturing porous material. Comput Methods Appl Mech Eng 2013;256:29–37.
[31] Cao DT, Milanese E, Remij EW, Rizzato P, Simoni L, Huyghe JM, et al. Interaction between crack tip advancement and fluid flow in fracturing saturated porous media. Mech Res Commun 2017;80:24–37.
[32] Tzschichholz F, Herrmann HJ. Simulations of pressure fluctuations and acoustic emission in hydraulic fracturing. Phys Rev E 1995;51:1961–70.